

STATISTICAL MODELING AND ANALYSIS OF STRUCTURES IN AORTA
IMAGES

A Dissertation

by

HAI XU

Submitted to the Office of Graduate Studies of
Texas A&M University
in partial fulfillment of the requirements for the degree of

DOCTOR OF PHILOSOPHY

August 2011

Major Subject: Computer Engineering

Statistical Modeling and Analysis of Structures in Aorta Images

Copyright 2011 Hai Xu

STATISTICAL MODELING AND ANALYSIS OF STRUCTURES IN AORTA
IMAGES

A Dissertation

by

HAI XU

Submitted to the Office of Graduate Studies of
Texas A&M University
in partial fulfillment of the requirements for the degree of

DOCTOR OF PHILOSOPHY

Approved by:

Chair of Committee,	Jyh-Charn Liu
Committee Members,	Jay D. Humphrey
	Yoonsuck Choe
	Dezhen Song
Head of Department,	Valerie E. Taylor

August 2011

Major Subject: Computer Engineering

ABSTRACT

Structural Modeling and Analysis of Structures in Aorta Images. (August 2011)

Hai Xu, B.S., Tsinghua University (China;)

M.S., Clemson University

Chair of Advisory Committee: Dr. Jyh-Charn Liu

Morphology change analysis of aorta images acquired from biological experiments plays a critical role in exploring the relationship between lamina thickness (LT), interlamellar distance (ILD) and fragmentation (furcation points) with respect to pathological conditions. An automated software tool now is available to extract elastic laminae (EL) and measure LT, ILD and fragmentation along their ridge lines in a fine detailed aspect. A statistical randomized complete block design (RCBD) and *F*-test were used to assess potential (non)-uniformity of LT and ILD along both radial and circumferential directions. Illustrative results for both normotensive and hypertensive thoracic porcine aorta revealed marked heterogeneity along the radial direction in nearly stress-free samples. Quantifying furcation point densities were also found that can offer new information about potential elastin fragmentation, particularly in response to increased loading due to hypertension.

Furthermore, when biological scientists analyze the elastic lamina structure, how to automatically generate a macro-level geometric parameter mapping might greatly help them understand the over-all morphology changes of blood vessel cross section. In this

dissertation, another automated system is designed to quickly locate more pronounced EL branches to construct layer level abstraction of LT/ILD measurements and transform the sparse pixel level information to dense normalized *Virtual Layer Matrix* (VLM). The system can automatically compute the EL orientations, identify pronounced ELs, transform the denoised LT measurement points onto a VLM and then provide statistics/segmentation analysis. By applying the k -means segmentation technique to VLMs of LT-ILD, one can easily delineate regions of normal vs. hypertrophic and/or hyperplasia LT-ILD measurements for cross-image references.

DEDICATION

To My Wife, Son, and Parents

ACKNOWLEDGEMENTS

I would like to thank Dr. Jyh-Charn Liu for his guidance, support and patience throughout my graduate study. He has been a constant source of inspiration and help. His suggestions and deep insight on academic domain knowledge contributed greatly to the completion of this dissertation, as well as to my academic achievements.

I would like also to express my appreciation to my committee members:

Dr. Jay D. Humphrey, Dr. Yoonsuck Choe, and Dr. Dezhen Song. They gave me very helpful suggestions on improving the quality of this dissertation. I am grateful to them for their guidance and support.

I also appreciate my dear wife, Hong Yu, and my parents for their dedication and patience. Without their support, I would not have finished my degree.

TABLE OF CONTENTS

	Page
ABSTRACT	iii
DEDICATION	v
ACKNOWLEDGEMENTS	vi
TABLE OF CONTENTS	vii
LIST OF FIGURES.....	ix
LIST OF TABLES	xii
CHAPTER	
I INTRODUCTION.....	1
II GEOMETRIC PARAMETERS MEASUREMENT AND STATISTICAL HYPOTHESIS VALIDATION	5
2.1 Image Preparation and System Flow Chart.....	5
2.2 Lamina Detection	8
2.3 Principal Direction of Elastic Laminae	12
2.4 Lamina Thickness Sampling Method, Estimation and Modeling	18
2.5 Aortic Fragmentation Measured via Furcation Point Densities	31
III VIRTUAL LAYER	38
3.1 Definition and Purpose of Virtual Layer.....	38
3.2 Log-Gabor Filter	44
3.3 Comparison between Gabor and Log-Gabor Filters	48
3.4 Searching Mechanism Definition of EL.....	51
3.4.1 Searching Criteria Definition	51
3.4.2 Aggregation of Multiple Search Routes.....	52
3.5 Virtual Layer Segmentation	56
3.6 Statistics Analysis and Hypothesis Test of LT and ILD Based on Virtual Layer Matrix	59

CHAPTER	Page
3.7 VLM Analysis and Discussion.....	62
3.7.1 VLM Statistics Analysis and Discussion	62
3.7.2 Comparison to Morphology Thinning Algorithm on Lamina Detection	64
IV CONCLUSION	69
REFERENCES	75
VITA	82

LIST OF FIGURES

	Page
Figure 1. Light microscopic images of representative cross-sections of porcine thoracic aorta in a nearly stress-free configuration in (a) normotension (NT) and (b) 4-week hypertension (HT).	6
Figure 2. Processing flow for automated elastic laminae structural analysis.	8
Figure 3. (a) A representative non-aligned portion of an aortic cross-section, (b) an intensity histogram for the red channel from the raw image (x-axis is the grayscale intensity range [0 255], y-axis is the counts of image intensity), (c) the binarized map highlighting the elastic laminae, with an adaptive threshold = 121 (black area), and (d) a skeleton map of the laminae with artifacts (black lines).	10
Figure 4. A synthetic binary image consisting of five sinusoidal curves was used to verify the accuracy of my Radon Transform (RT) algorithm.	14
Figure 5. Computed angle for the principal (circumferential) direction estimated by the LF-based method for the aortic image in Figure 3a, using different laminae skeleton length thresholds.....	16
Figure 6. Homogeneity test using both a Randomized Complete Box Design (RCBD) and a statistical F-test.....	19
Figure 7. Computed elastic laminae thicknesses (a, b) and inter-lamellar distances (c, d) within the medial layers of representative normotensive (a,c) and 4-week hypertensive (b,d) thoracic aorta.	25
Figure 8. Regional, spatial non-uniformities of the laminae thickness (LT) illustrated by a simple thresholding routine: (a) and (b) below average ($LT < \mu - \sigma$), (c) and (d) average ($\mu - \sigma < LT < \mu + \sigma$), and (e) and (f) above average ($LT > \mu + \sigma$). In above figures, (a), (c) and (e) are outcomes of NT. (b), (d) and (f) are outcomes of HT.	28
Figure 9. (a) Furcation Point (FP) Analysis using 22 standard templates. (b) Furcation points detected from skeleton lines for a representative magnified local section from an aortic image.	32

	Page
Figure 10. Furcation point area (line) density boxplots of data from Table 6. Both computations include five categories: surgery control (SC) and two-, four-, six- and eight-week HT aortic samples. X-axis shows the categories, y axis demonstrates the FP area (left) and line (right) densities.	34
Figure 11. Furcation point (FP) area density measurements with a running average (window size is five) for representative (a) normotensive and (b) 4-week hypertensive samples.	36
Figure 12. Computing steps for automated generation of VLM for an aorta image.	41
Figure 13. (a) An aorta image. In this image, ELs on the left side are thinner than those on the right side. (b) Automatically generated starting points (cross marks in green), and ELs (yellow lines). (c) Color coded LT map for LT values on EL ridge lines. d) The VLM of the LT map.	42
Figure 14. (a) An original image, on which white regions represent EL, and black regions for smooth muscle cells and collagen. (b) The Log-Gabor map of the image. (c) a zoom-in view of a cropped area of (b). Red arrows show the local tissue orientation computed through LGF. If the local orientation is zero, it will show as one red dot.	45
Figure 15. LGF based algorithm is robust to noises. (a) and (a') are two different aorta cropping. (b) and (b') are the orientation map. For a better visual effect, in (b) and (b'), only the directions on the ELs are shown in the figure. In (c),(c'), (e) and (e'), Gaussian noises with $\sigma = 0.1$ and 0.5 were applied to (a) and (a'). (d), (d'), (f) and (f') are their orientation map respectively.	46
Figure 16. EL flow direction detection results by (a) Gabor filter, and (b) Log-Gabor filter.	50
Figure 17. Aorta image with searched ELs highlighted with yellow	52
Figure 18. Multi-route issue: when searching the EL skeleton, based on different starting points, the searching results might be different.	53
Figure 19. Simulation of pixel intensities within an analysis window. The intensity distribution distributes similar to a Gaussian.	54

	Page
Figure 20. Multi-route issue solution: in above figures (a) and (b), five different starting points are randomly and sequentially selected.	55
Figure 21. Porcine aorta LT morphology differences highlighted with k-means segmentation outcomes from VLM. (a) is a NT image, (b) is a HT sample, (c) and (d) are the generated VLM with Matlab pseudo color. Red represents high-value thickness and blue represents low-value. Green is a value in-between. (e) and (f) are the segmentation outcomes from k-means technique with three clusters pre-defined. Red color highlights the significantly thickened region. (g) and (h) are the outcomes by applying morphology operations (dilatation and removal) to smooth the segmentation outcomes. (i) and (j) are the smoothed segmentation outcome imposed over original images.	57
Figure 22. Averaged VLM boxplots of data from averaged LT/ILD values of VLM.	60
Figure 23. Averaged VLM boxplots of data of thickened (a) LT ratio and (b) ILD ratio.	61
Figure 24. Two aorta images (first row), their EL maps obtained using a morphology thinning algorithm (second row), and ELs by LGF-based search using manually selected initial points.	66
Figure 25. EL detection result comparison between morphology thinning algorithm and Log-Gabor Filter based algorithm.	67

LIST OF TABLES

	Page
Table 1 Comparison of principal directions determined by manual and automatic measurement.....	13
Table 2 Comparison between the given principal direction and outcomes from RT and LF algorithms.	15
Table 3 Computation time and accuracy comparison between LF and RT-based algorithms.....	17
Table 4 Statistical Randomized Complete Block Design (RCBD) for hypothesis testing of equal measurement means.....	20
Table 5 ANOVA tables for normotension and 4-week hypertension LT and ILD data.....	23
Table 6 Area and line density of furcation points corresponding to Figure 10.....	33

CHAPTER I

INTRODUCTION

In hypertension, the arterial walls subjected to elevated blood pressure undergo marked growth and remodeling (G&R) processes that modify wall characteristics, especially the thickness [1-3]. Of the many structural constituents that make up the arterial wall, elastin plays a particularly important role in large arteries. Elastin endows these arteries with considerable distensibility, elasticity, axial prestretch, and overall durability; it similarly provides important biological cues for associated smooth muscle cells to remain quiescent and contractile [4, 5]. Not surprisingly, therefore, mounting laboratory and clinical evidence shows that damage to or loss of elastin contributes significantly to many arterial pathologies. For example, fatigue-induced fragmentation and degeneration of elastin are major contributors to the increased caliber, neointimal thickening, tortuosity, and stiffening that are hallmarks of arterial aging [6, 7], and thereby contribute to the associated increased pulse pressure and risk of heart attack, stroke, and kidney failure [8, 9]. Indeed, similar changes in elastin cause or are caused by hypertension and thereby contribute to its devastating role in the progression of many cardiovascular diseases [10]. Increasing evidence also suggests that a deficiency of fibrillin-1 (an elastin associated glycoprotein) in people having Marfan syndrome renders the arterial elastin more susceptible to degeneration and enzymatic degradation

[11], which in turn contributes to dilatation and eventual dissection of the ascending aorta. Degradation and loss of elastin is similarly thought to play a key role in the pathogenesis and subsequent enlargement of both abdominal aortic and intracranial aneurysms [12, 13], and it appears to play a role in both the development of atherosclerosis [14] and the restenosis that often follows balloon angioplasty or intravascular stenting [15]. There is, therefore, a pressing need to quantify changes in elastin organization within the arterial wall.

The dynamic behaviors of such changes require consistent, automated measurement techniques, to assess relationships between biomechanical and functional changes. Recently developed porcine aortic coarctation model was used to study hypertension-induced G&R [1]. The porcine aorta represents a better choice than rodent arteries for studying potential stress-induced G&R because they have more elastic laminae across the vessel wall. The porcine vasculature is also more similar to that of humans in comparison to that of rodents.

The altered circumferential wall stress in early hypertension is often hypothesized to be a key initiator of G&R. Medial SMCs, embedded in an abundant extracellular matrix, bear part of the initially increased circumferential stress. These cells may undergo hypertrophy (i.e., increased cell size) and/or hyperplasia (i.e., increased cell number), and they may abnormally synthesize and deposit different matrix proteins (e.g. collagen and elastin) as well as matrix metalloproteinases (MMP) and tissue-inhibitors of MMPs (TIMP), which further regulate matrix turnover. Each of these processes plays an active role in G&R of the arterial wall. It is possible that the medial

SMCs may respond differently, based on their radial location in the arterial wall, to the altered stress/strain gradient or the growth factor concentration gradient due to hypertension. That is, the synthesis and deposition of matrix proteins, including elastin, may start to increase in the inner media at the onset of increasing blood pressure and progress to the outer media through the development of hypertension. As the tensile stress borne by the SMCs re-normalizes to its homeostatic value, due to enhanced laminar units, the G&R may cease.

To validate these and many other hypotheses, an objective, quantitative measurement technique is needed for elastic laminae (EL) thickness across the arterial wall. In this dissertation, I propose an image analysis scheme to delineate spatial patterns of EL such as changes in its thickness across the arterial wall. Key features of my scheme include: 1) a Radon Transform based technique for automated orientation of the principal direction of EL, 2) localized measurement techniques for lamina thickness (LT), interlamellar distance (ILD), and lamina intensity gradient and 3) furcation point (FP) detection technique and density spatial distribution measurements, (4) statistical based experimental design to validate hypotheses related to regional non-uniformity of the elastic laminae in aorta, (5) Log-Gabor filter (LGF) based local greedy EL searching algorithm, and (6) An dense matrix abstraction for sparse pixel level measurements of LT/ILD. The approach presented in this dissertation thus enables a fully automated analysis system that includes EL extraction, alignment, point-wise and transmural thickness measurement, regional level analysis of virtual layer matrix (VLM) for macro-domain aspect, and statistical hypothesis testing to assess the (non)-uniformity of LT and

ILD. The uniformity analysis of LT complements the homogeneity analysis of elastic laminae based on mechanical experiments [16]. It is also shown here that although automatic alignment of arterial sections by principal direction of elastic laminae is complicated by their inherent waviness, sectioning artifacts, and arbitrarily oriented specimens, a RT based algorithm can align histological images (typically 1500x2000 or larger) faster than traditional approaches such as linear fitting [17], eigenvector/eigenvalue analysis [18], and texture orientation measurement methods [19-23].

CHAPTER II
GEOMETRIC PARAMETERS MEASUREMENT AND STATISTICAL
HYPOTHESIS VALIDATION*

2.1 Image preparation and system flow chart

Cylindrical segments of excised porcine thoracic aorta from another study [1] were cut to release residual stresses and processed using standard histological methods (e.g., embedded, sectioned, and stained). Sections were stained with Verhoeff Van Gieson (VVG) to focus on intramural elastin (the main component of elastic laminae). Images were acquired using a research light microscope (Olympus BX51) coupled with a digital camera (Olympus DP70). The 1360 x 1024 digitized images were taken at 1/500 second exposure time, ISO 200 sensitivity, and 20x zoom. When necessary, the “PanaVue Image Assembler” was used to stitch together snapshots to form a whole section of the aortic wall. All images were rotated into the same sequence of the three main layers (left to right): adventitia (outer layer), media (middle layer), and intima (inner layer), with attention directed primarily to the elastin-rich media (Figure 1). Note, therefore, that the elastic laminae are represented by the dark lines in Figure 1 whereas the pink/purple denotes remaining constituents, primarily collagen, smooth muscle, and ground substance matrix. The overall processing flow of the automated analysis system is depicted in Figure 2.

*Reprinted with permission from “Automated measurement and statistical modelling of elastic laminae in arteries” by Hai Xu, Jin-Jia Hu, Jay D. Humphrey and Jyh-Charn Liu, 2010. *Computer Methods in Biomechanics and Biomedical Engineering*, Vol. 13, No. 6, 749–763, Copyright 2010 by Taylor and Francis.

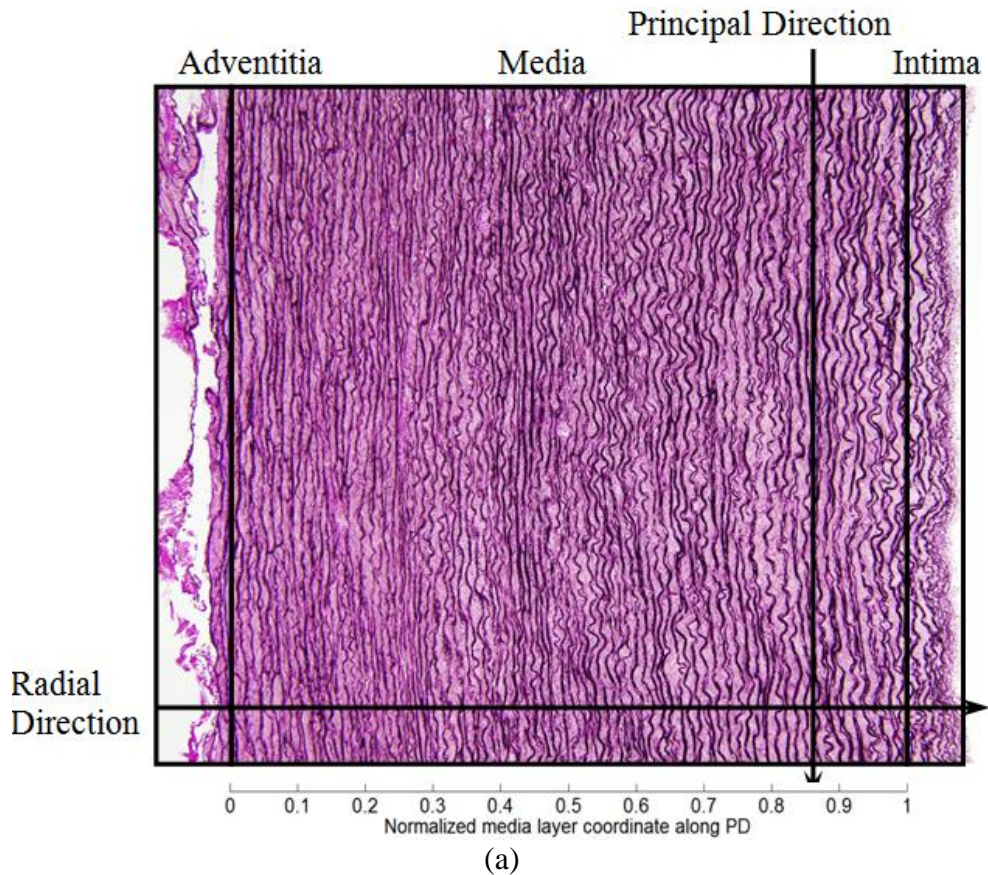


Figure 1. Light microscopic images of representative cross-sections of porcine thoracic aorta in a nearly stress-free configuration in (a) normotension (NT) and (b) 4-week hypertension (HT). Note the typical tri-layered structure (adventitia, media, and intima). The intramural constituents include the concentric elastic laminae (dark lines) and intralamellar smooth muscle, collagen, and ground substance (pink). Two delimiting elastic laminae and the enclosed tissue define the basic structural and functional unit of the wall, a musculo-elastic fascicle or lamellar unit. The principal (circumferential) direction runs along the trajectory of elastic laminae whereas the perpendicular (radial) direction runs radially from intima to adventitia.

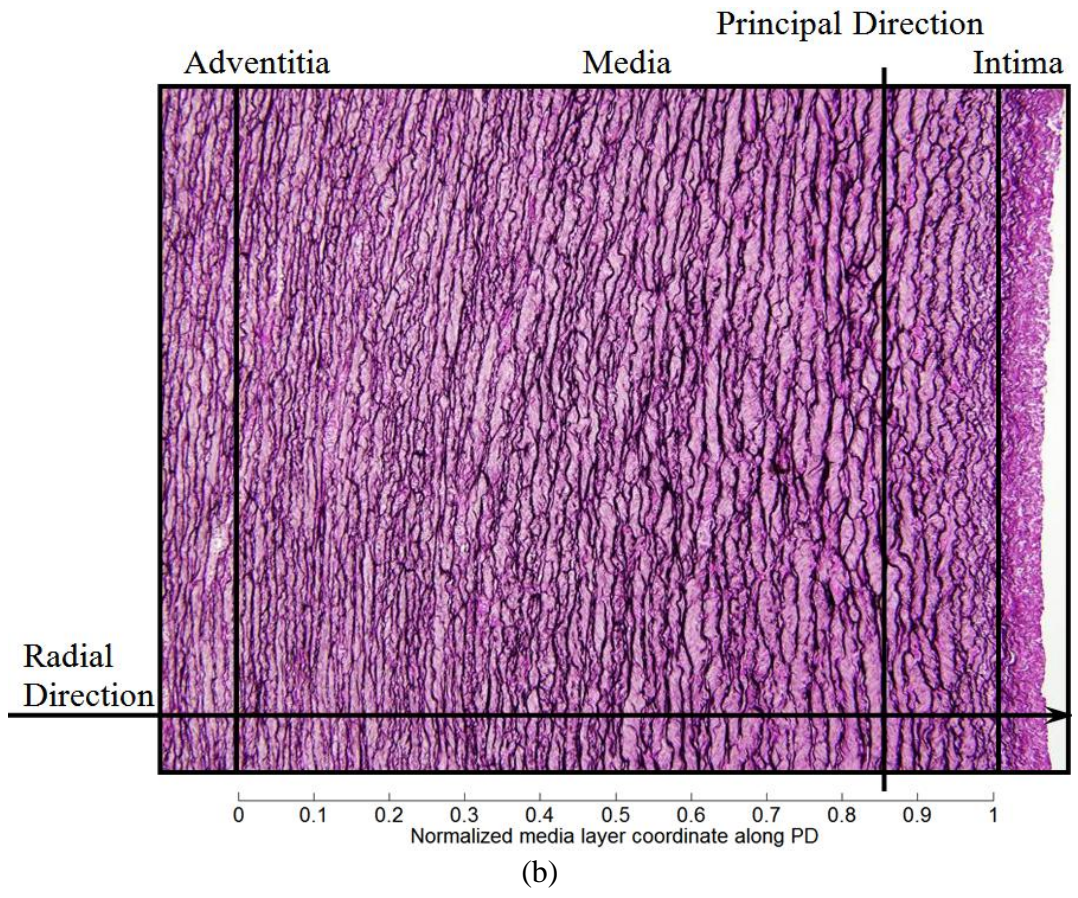


Figure 1. Continued

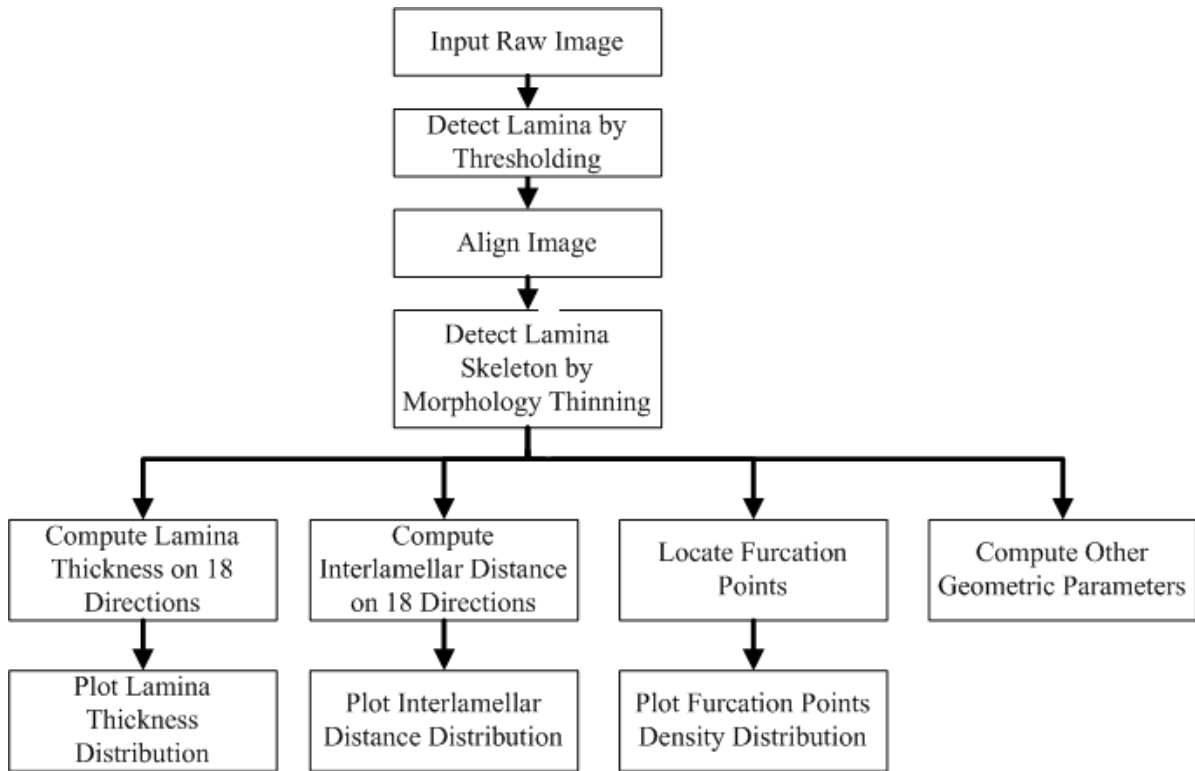


Figure 2. Processing flow for automated elastic laminae structural analysis.

2.2 Lamina detection

It is relatively simple to extract elastic laminae from an original image when there is a sharp contrast between each lamina (foreground) and the non-elastic lamellar (background) constituents, particularly in the red channel of color images (Figure 3a).

Yet, different threshold selections can yield different segmentation outcomes. For example, referring to a histogram for a representative histological sample (Figure 3b), there is a clear, but not distinct, boundary between foreground and background. To avoid the need for manual selection and decisions on the appropriate dividing threshold, I

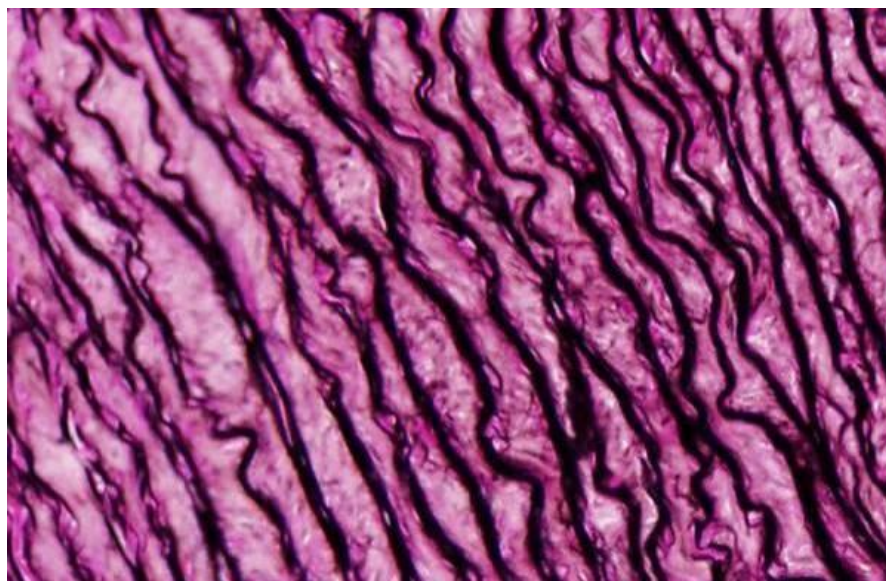
adopted an adaptive threshold method [24] to segment the foreground (elastic laminae) and background:

1. Empirically set an initial threshold I_0 to 140.
2. Segment image pixels as foreground or background based on I_0 .
3. Compute the average intensity of pixels in the foreground as I_1 and that of background as I_2 .

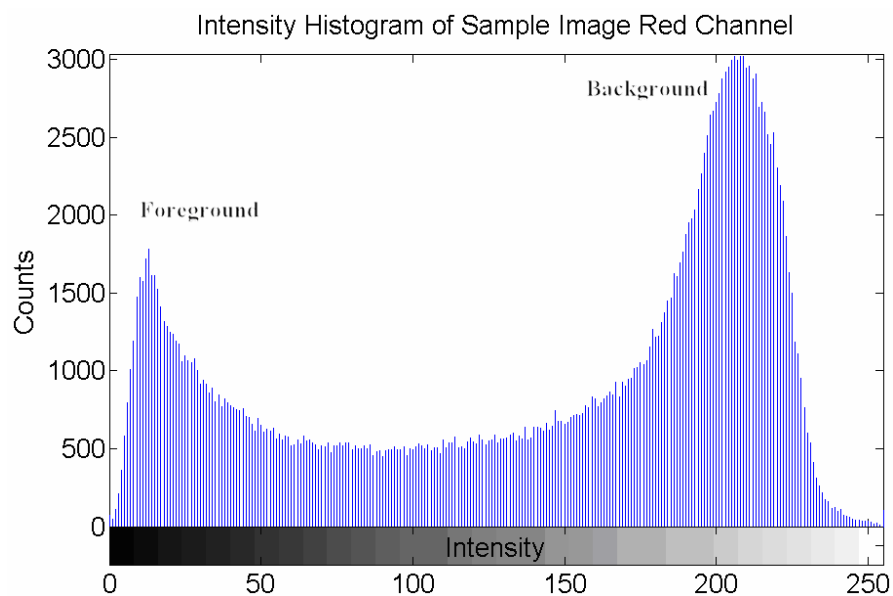
4. Compute a new threshold $I'_0 = \frac{(I_1 + I_2)}{2}$.

5. If $|I_0 - I'_0| < 1$, then stop. Else, let $I_0 = I'_0$ and go back to step 2.

Next, I'_0 was used as a threshold to eliminate the background and generate a binarized map of the elastic laminae (Figure 3c). Small laminae (≤ 20 pixels) were assumed to be cutting artifacts or marginal tissues, and were either removed (laminae) or filled (inter-lamellar regions) with a seed fill [24]. Centerlines (skeleton) of the elastic laminae (Figure 3d) were then extracted using a mathematic morphology based thinning algorithm [25, 26]. Once this step was completed, it was then possible to determine the mean principal direction (i.e., direction of primary “flow”, typically circumferential in an artery) of the elastic laminae (Figure 1) and then to determine other metrics of interest along the perpendicular direction (typically radial in an artery). The associated techniques to compute these metrics are discussed in order below.

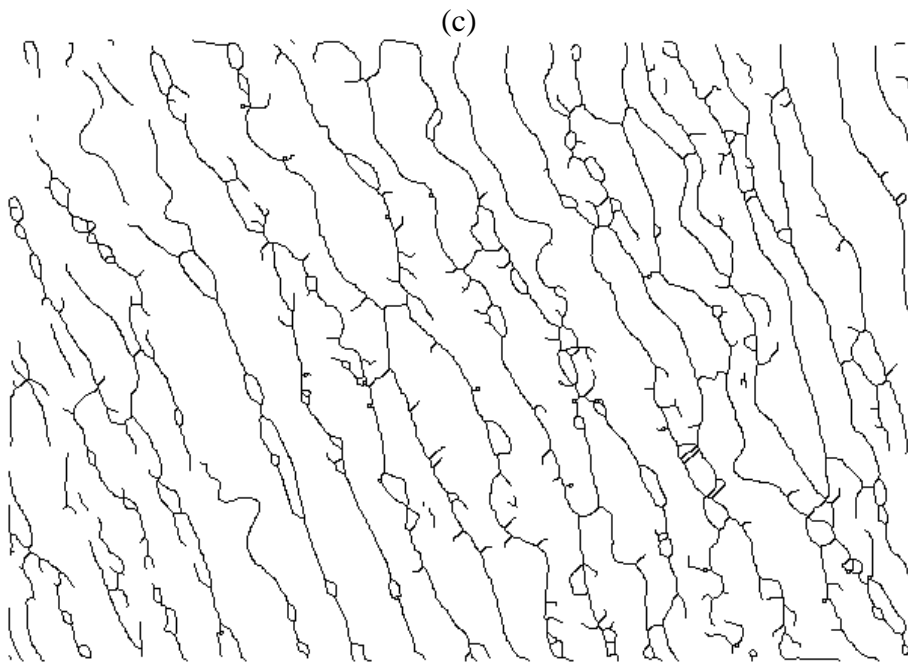
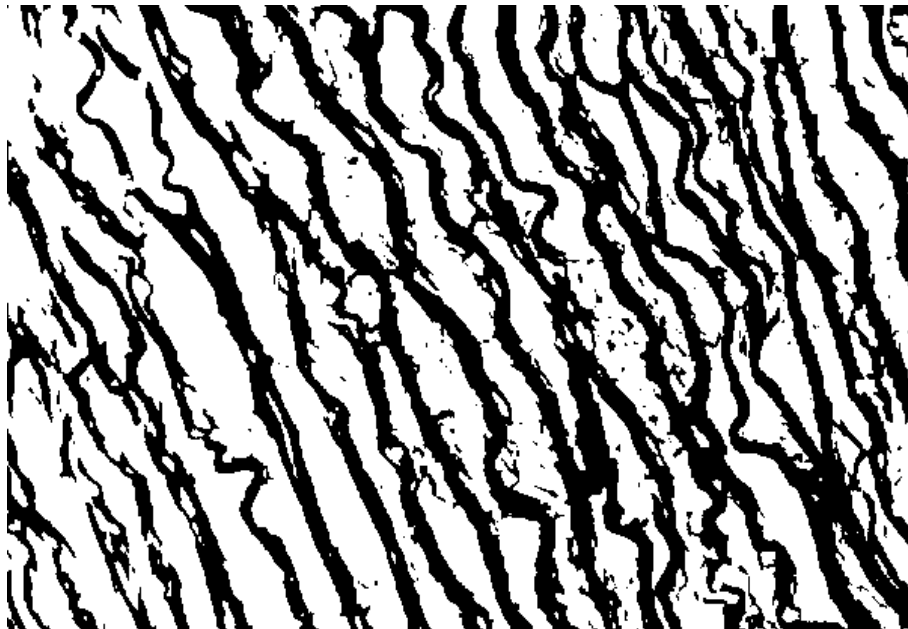


(a)



(b)

Figure 3. (a) A representative non-aligned portion of an aortic cross-section, (b) an intensity histogram for the red channel from the raw image (x-axis is the grayscale intensity range [0 255], y-axis is the counts of image intensity), (c) the binarized map highlighting the elastic laminae, with an adaptive threshold = 121 (black area), and (d) a skeleton map of the laminae with artifacts (black lines).



(d)

Figure 3. Continued

2.3 Principal direction of elastic laminae

In [27], I proposed an algorithm using an energy function derived from the well-known RT (Radon Transform) to find the principal laminae direction, which is defined as the majority flow direction. The energy function was defined as:

$$e(\theta) \text{ RT } f(x, y) = \left\| \nabla \text{ RT}_\theta f(x, y) \right\|^2, \quad (1)$$

where $\nabla(\cdot) = d(\cdot)/d\theta$, f is a function, (x, y) is the coordinate of a laminae point, and θ is the radon transform projection angle. By modelling elastic laminae as rectangular objects, the RT-based energy function becomes

$$E_{RT}(x, y) = \int_{-\infty}^{\infty} \left[\frac{dg_{\Pi}(x, y)}{dr} \right]^2 dr, \quad (2)$$

where r is the perpendicular distance from the origin to the straight line, with integration limits to infinity based on definition of radon transform, and

$$g_{\Pi}(x, y) = \tan \theta \left\{ \text{sgn} \left[p \csc \theta + b \text{ ctg} \theta a \right] \min \left[|p \csc \theta + b|, |\text{ctg} \theta a| \right] - \text{sgn} \left[p \csc \theta - b \text{ ctg} \theta a \right] \min \left[|p \csc \theta - b|, |\text{ctg} \theta a| \right] \right\}, \quad (3)$$

where $\tan(\cdot)$ is the tangent function, $\text{sgn}(\cdot)$ is the sign function, $\csc(\cdot)$ is the cosecant, $\text{ctg}(\cdot)$ is the cotangent function, a is a constant which is obtained from the rectangle function, with distance p and angle θ defining the straight line.

To verify the accuracy of my automatic method, I randomly picked 40 sample images and a “blinded” expert manually selected a principal direction three times. Differences between the average results for the manual and automatic methods are summarized in Table 1. The mean and standard deviation of the differences is 1.6 ± 1.0 degrees.

Table 1. Comparison of principal directions determined by manual and automatic measurement.

Sample #	1	2	3	4	5	6	7	8	9	10
Measure 1	-25	-16	-16	24	28	13	15	-12	23	25
Measure 2	-24	-14	-14	25	29	12	16	-10	28	28
Measure 3	-25	-13	-13	25	28	13	15	-10	21	22
Auto Measurement	-24	-12	-12	26	27	14	15	-10	26	22
Difference	0.7	2.3	2.3	1.0	1.0	1.3	0.3	1.0	2.0	3.0
Sample #	11	12	13	14	15	16	17	18	19	20
Measure 1	21	-22	-20	-19	-9	8	11	10	14	18
Measure 2	22	-21	-21	-18	-10	9	12	12	15	19
Measure 3	21	-23	-23	-20	-10	10	11	11	15	20
Auto Measurement	25	-19	-19	-18	-9	10	9	9	15	18
Difference	3.7	3.0	2.3	1.0	0.7	1.0	2.3	2.0	0.3	1.0
Sample #	21	22	23	24	25	26	27	28	29	30
Measure 1	15	17	10	5	21	-31	-28	-41	-20	11
Measure 2	14	16	11	4	25	-30	-25	-40	-21	11
Measure 3	14	17	11	3	23	-30	-24	-40	-19	10
Auto Measurement	13	18	11	1	20	-29	-23	-43	-22	10
Difference	1.3	1.3	0.3	3.0	3.0	1.3	2.7	2.7	2.0	0.7
Sample #	31	32	33	34	35	36	37	38	39	40
Measure 1	-20	15	-25	-23	-26	23	-22	-14	-10	-15
Measure 2	-24	17	-26	-21	-27	24	-20	-15	-9	-11
Measure 3	-23	17	-27	-22	-27	25	-23	-15	-10	-13
Auto Measurement	-20	16	-26	-22	-23	23	-19	-12	-9	-12
Difference	2.3	0.3	0.0	0.0	3.7	1.0	2.7	3.0	1.0	1.0

Furthermore, I tested the RT algorithm and evaluated its accuracy by comparing results to those for a LF (linear fitting) [17] algorithm using a known, synthetic binary image (Figure 4). Each curve within the synthetic image was created using five different functions so that their shapes resemble that of elastic laminae. The functions are (from top to bottom):

$$\begin{aligned}
y_1 &= 0.6 \sin(0.5x) + 0.25 \sin(0.3x - 3) + \sin(0.1x - 4) \\
y_2 &= 0.6 \sin(0.5x - 3) + 0.25 \sin(0.3x + 3) + \sin(0.1x - 4) \\
y_3 &= 0.3 \sin(0.6x - 3) + 0.5 \sin(0.71x - 3) + 0.9 \sin(0.21x + 4) \\
y_4 &= 0.36 \sin(0.7x - 1) + 0.75 \sin(0.41x - 2) + 0.27 \sin(0.25x + 1) \\
y_5 &= 0.41 \sin(0.19x - 1) + 0.5 \sin(0.51x + 2) + 0.3 \sin(0.65x - 1).
\end{aligned} \tag{4}$$

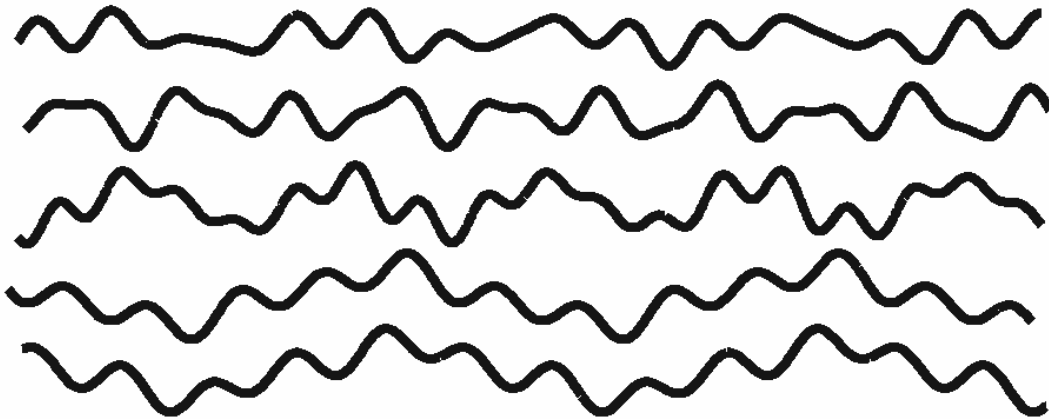


Figure 4. A synthetic binary image consisting of five sinusoidal curves was used to verify the accuracy of my Radon Transform (RT) algorithm. The principal directions of all curves were forced to be 0° from horizontal, but the image was rotated by 30° , 60° , 90° , 120° , 150° or 180° for different tests. After repeating ten times for each rotation, averaged outcomes for both RT and linear fitting (LF) algorithms were compared to assess their accuracies.

All of the synthetic curves were created so that their principal directions had an initial zero degree orientation relative to horizontal. I then generated test images by rotating the original images from 30° to 180° , in 30° increments. Averages of ten experimental runs for RT and LF fitting methods are in Table 2, which reveals that the RT algorithm was consistently more accurate than the LF algorithm as expected.

Table 2. Comparison between the given principal direction and outcomes from RT and LF algorithms. Column one is the rotated degrees of Figure 4 from the prescribed principal direction. Columns two and four are, respectively, the principal directions computed by the LF and RT algorithms. The accuracies $(\theta_1 - \theta_0)/\theta_0$ are listed in columns three and five as percentages.

True Rotation Degree $\theta_0(^{\circ})$	LF result θ_1 ($^{\circ}$)	LF Accuracy (%)	RT result θ_2 ($^{\circ}$)	RT Accuracy (%)
30	30.11	0.4	30	0.0
60	59.9	-0.2	60	0.0
90	94.2	4.7	92	2.2
120	120.51	0.4	120	0.0
150	150.31	0.2	150	0.0
180	180.17	0.1	180	0.0

Furthermore, I chose five “representative” aortic cross-sectional images having the same resolution but different dimensions to compare the performance of these two methods. The LF scheme generated principal directions with good accuracy when the threshold for the laminae skeleton length (cf. Figure 3d) was selected properly. Figure 5 illustrates the relationship between skeleton length threshold and estimated principal direction (for Figure 3a) using the LF method, with the threshold chosen to be 10 to 65 pixels with a 5-pixel increment. Maximum and minimum values were 27.02° and 35.89° , that is, about 8° different. Indeed, the estimated principal direction tended to a converged value even for large thresholds (> 40). Proper parameter selection for the LF-based algorithm is not an easy task, however. In contrast, the RT-based algorithm does not require thresholding; the input can be a grayscale image and the RT-based algorithm is shift-, rotation- and scale-free. I always obtained little error in the numerical experiments when removing any combination of the five curves.

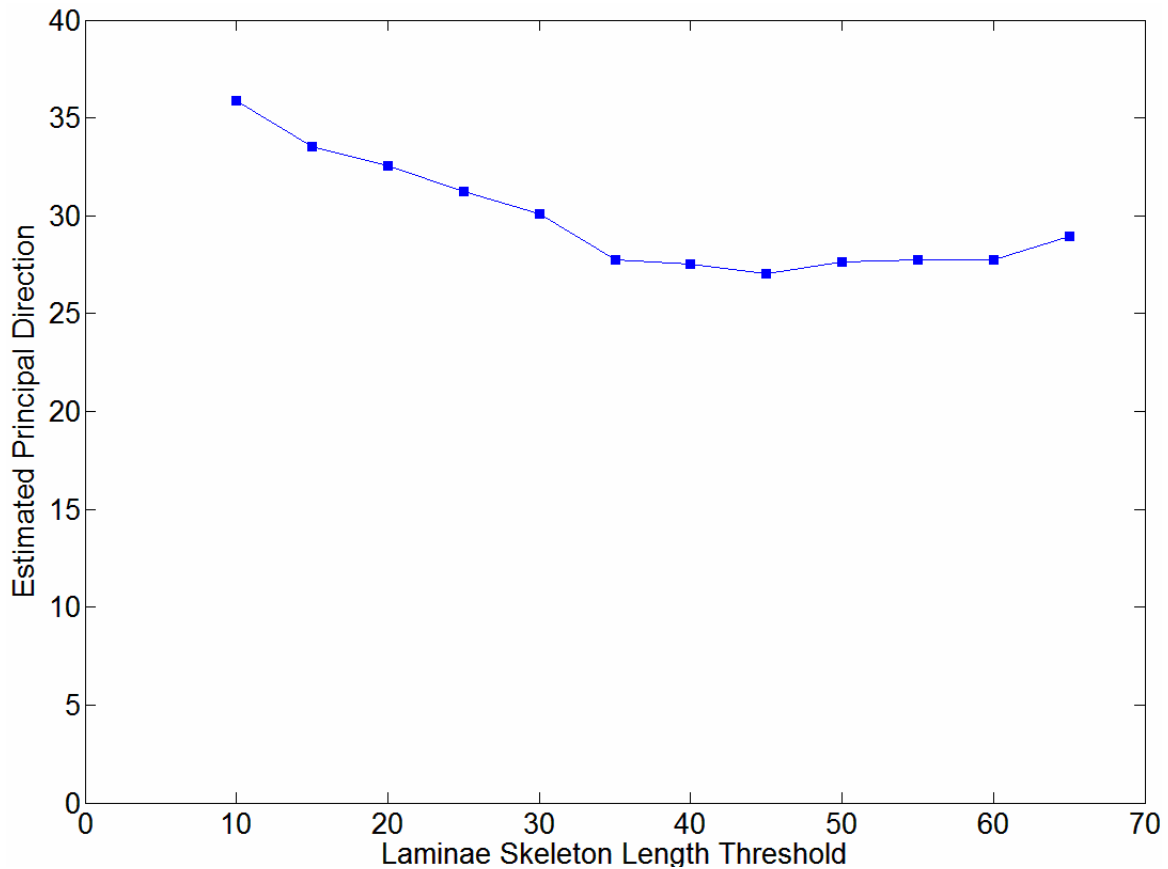


Figure 5. Computed angle for the principal (circumferential) direction estimated by the LF-based method for the aortic image in Figure 3a, using different laminae skeleton length thresholds. The largest and smallest angles were 35.89° (threshold 10 pixels) and 27.02° (threshold 45), respectively. The associated parameter-insensitive angle computed using the RT method was 27° .

Finally, when smaller laminae were removed based on a length threshold of 20 pixels, the remaining laminae skeleton was fit to a linear equation having slope k and y -intercept b (i.e., $y = kx + b$). The direction of every fit line is $\tan^{-1}(k)$. With all laminae fit, I chose the median value of all directions as the principal direction of the elastic laminae within the cross-sectional image. Accuracies and computing times for the RT-based algorithm were compared against the LF-based method (Table 3), with

computation time averaged over the five different runs for each image. As it can be seen from the table, the RT-based method also had a marked speed gain over the LF counterpart. Given that most aortic images are large (e.g., 1360 x 1024), the RT-based method was found to be more suitable for large scale experiments.

Table 3. Computation time and accuracy comparison between LF and RT-based algorithms. Column one is the number of sample images and their sizes (measured by pixel count). Columns two and three are the computing times for the two algorithms: linear fitting (LF) and Radon transform (RT). Columns five and six are the angles of the principal directions (PD) computed by the two algorithms. The last column is the difference between the results of the two methods. Despite similar accuracies, the RT based method outperformed the LF method because of its lower processing time for large images.

Sample (dimension)	Computing Time			Measurement Results		
	LF Method Time t_1 (sec)	RT Method Time t_2 (sec)	Time Ratio (t_2/t_1)	PD from Linear Fitting P_1 (°)	PD from RT P_2 (°)	PD error ($P_1 - P_2$)
1 (563 x 500)	4.565	5.97	1.31	78.5	80	-1.5
2 (637x474)	5.025	6.71	1.33	88.2	87	1.2
3 (806x744)	14.33	14.25	0.99	81.8	81	0.8
4 (1866x1372)	118.78	66.32	0.56	77.5	77	0.5
5 (2513x1382)	199.47	107.2	0.54	83.8	83	0.8

2.4 Lamina thickness sampling method, estimation, and modeling

I adopted the definitions of LT (laminae thickness) and ILD (inter-lamellar distances) from [28], where LT is the shortest distance between two elastic laminae boundaries and ILD is the shortest distance between two neighboring laminae, and I used the method in [29] to measure the LT and ILD. Point-wise measurements of LT were based on a local search method along 18 directions within the cross-sectional image plane [27]. The ILD can be measured similarly for regions between neighboring elastic laminae. To verify the accuracy of this method, I randomly picked 97 points from seven different sample images. I compared the manual IL measurement with the automatic method; the difference was 0.4 ± 0.3 pixels, which showed the reliability of my algorithm.

A more challenging issue, however, was to assess the (non)-uniformity of LT distributions across different regions. If LT was mostly homogenous, a simple average of all point-wise measurements would suffice. Otherwise, regional measurements of LT would be required to study structural characteristics of LT across the wall. Because one can derive an overall average from regional measurements, I based my study on regional analysis techniques. Specifically, to determine possible regional homogeneities, one could first divide each image using r uniform vertical blocks that have the same heights as the image height, and then analyze the LT statistics in each block. Because such blocks could have different numbers of observations, however, this naïve approach could lead to biased statistical estimations. To eliminate such potential biases, I employed a randomized complete block design (RCBD) [30, 31] with a fixed number t of samples in

each block to test the homogeneity hypothesis. RCBD is one of the simplest blocking designs to control and reduce experimental errors. My analysis is confined to a 1D (vertical or horizontal) homogeneity analysis and consists of two steps (Figure 6): RCBD and standard F-test checks of homogeneity.

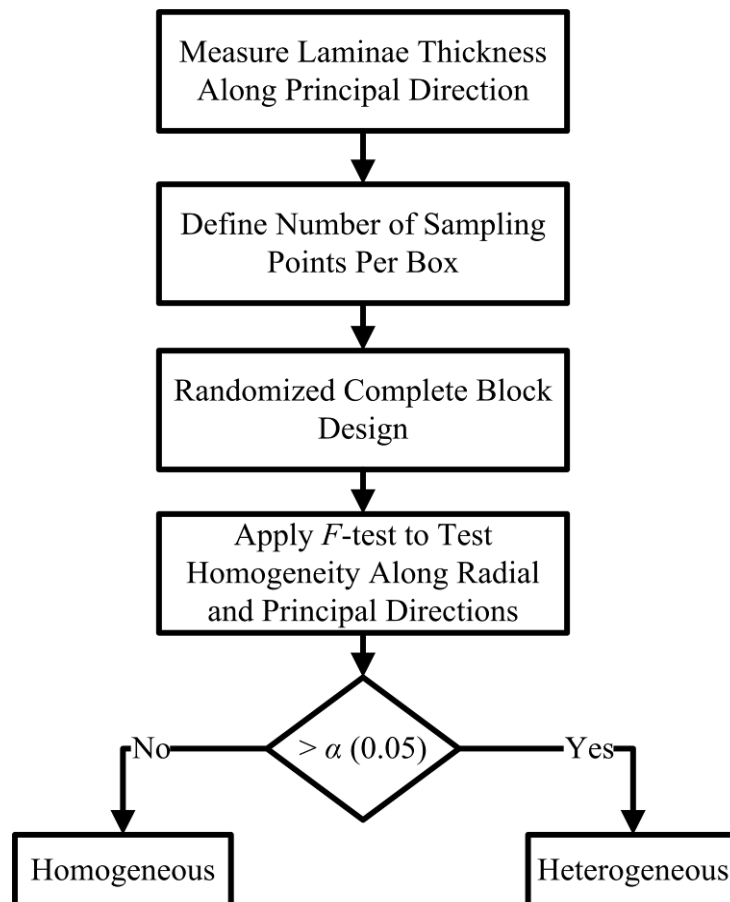


Figure 6. Homogeneity test using both a Randomized Complete Box Design (RCBD) and a statistical F-test.

Based on the central limit theorem, one can assume that the measurement L over a homogenous area to be an independent and identically distributed random variable with a small standard deviation. For a randomly selected number t (not independent and identically distributed in different areas) of samples L_1, L_2, \dots, L_t within an analysis region w , the measurement mean $\bar{L} = \frac{1}{t} \sum_{i=1}^t L_i$ approaches that for a Normal distribution $N(\mu, \sigma(t))$, where μ and $\sigma(t)$ are the usual mean and standard deviation. Equal size t can help yield reasonably small variance in all analysis areas. The aforementioned RCBD method was thus applied to reduce variations for experimental results on the distributions of transmural metrics of interest. The parameters for the RCBD are summarized in Table 4.

Table 4. Statistical Randomized Complete Block Design (RCBD) for hypothesis testing of equal measurement means. The sample images are divided into r vertical regions (blocks) with heights equal to the image height. In each region, I randomly pick t measurements, e.g., LT or ILD. y_{ij} is the j th measurement in the region i . $\bar{y}_{i\cdot}$ is mean of i th measurement within all regions, $\bar{y}_{\cdot j}$ is mean within region j , and $\bar{y}_{\cdot\cdot}$ is estimated true means of all measurements.

Measurement	Region 1	Region 2	...	Region r	Measurement-means
1	y_{11}	y_{12}	...	y_{1r}	$\bar{y}_{1\cdot}$
2	y_{21}	y_{22}	...	y_{2r}	$\bar{y}_{2\cdot}$
...
t	y_{t1}	y_{t2}	...	y_{tr}	$\bar{y}_{t\cdot}$
Block means	$\bar{y}_{\cdot 1}$	$\bar{y}_{\cdot 2}$...	$\bar{y}_{\cdot r}$	$\bar{y}_{\cdot\cdot}$

In particular, I partitioned the medial layer into r non-overlapped columns (blocks) with the number of entries equaling the image height. In each region, I randomly picked t measurements (rows) where $t = 10\bar{n}$ and \bar{n} is the average number of sampling points over r regions within the whole image. Because the physical width of the regions could become unequal, the same number t of samples was used in each observation. I then applied a linear model for the i^{th} parameter measurement (i.e., diagnostic metric) within the j^{th} analysis region (block):

$$y_{ij} = \mu + \tau_i + \rho_j + e_{ij}, \quad (5)$$

where $i = 1, 2, \dots, t$, $j = 1, 2, \dots, r$, μ is the true measurement mean, τ_i is the treatment effect which explains how much a measurement changes on an experimental unit and e_{ij} is the measurement error. The block effect ρ_j is the average deviation of L from μ within each analysis region (block) j . Recall that the number of analysis regions is r and the number of sampling points in each region is t . For simplicity, I assumed random sampling point locations. The measurement error e_{ij} was thus assumed to be distributed normally with zero mean and a common variance. The F statistic [30] used to test hypothesis H_0 was:

$$F_0 = \frac{MST}{MSE} = \frac{r \sum_{i=1}^t (\bar{y}_{i\cdot} - \bar{y}_{\cdot\cdot})^2 / (t-1)}{\sum_{i=1}^t \sum_{j=1}^r (y_{ij} - \bar{y}_{i\cdot} - \bar{y}_{\cdot j} + \bar{y}_{\cdot\cdot})^2 / [(r-1)(t-1)]}, \quad (6)$$

where $\bar{y}_{i\cdot}$ is i^{th} measurement mean, $\bar{y}_{\cdot\cdot}$ is the estimated general mean, $\bar{y}_{\cdot j}$ is the j^{th} block mean, and y_{ij} is the measurement at i^{th} location and j^{th} block.

I used ANOVA [30] (analysis of variance) statistics to analyze results for LT and ILD in regions derived from the RCBD. The F statistic was used to test the null hypothesis H_0 :

$$H_0: \mu_1 = \mu_2 = \dots = \mu_i, \quad (7)$$

where μ_i is the mean of LD or ILD at block i . I wanted to test whether or not there were significant differences between the measurement means along the principal (or, circumferential) and radial directions at a significant level $\alpha = 0.05$. The test statistic α is the probability of exceeding the value of the test under the null hypothesis. The value labeled $Prob > F$ in the last column of Table 5 is often referred as the “ P -value”. In this dissertation, I chose the traditional significance level 0.05.

A detailed analysis of LT and ILD was completed for one representative normotensive (NT) and one 4-week hypertensive (HT) sample (Table 5). For both NT and HT, I found LT to be significantly different among blocks ($F = 0 < \alpha$) at $\alpha = 0.05$, which implied that LT was not distributed uniformly along the radial direction. In contrast, the F -statistics for LT and ILD were all larger than $\alpha = 0.05$ which suggested that LT or ILD were distributed uniformly along the circumferential direction for both the NT and 4-week HT cases. Their F -statistics are 0.9687, 0.2377, 0.9794 and 0.9916 respectively.

Table 5. ANOVA tables for normotension and 4-week hypertension LT and ILD data. ANOVA (analysis of variance) in Table 5 (a-d) test the homogeneity of LT or ILD under normotension (NT) and hypertension (HT) along different directions. Column six explains the probability of homogeneity. If the probability is larger than α , I cannot reject the null hypothesis (no significant differences between the measurement means along the principal (circumferential) or radial direction) at α level. Otherwise, I might conclude heterogeneity. In rows two and three of each table, the block and row effects test the homogeneity along the radial and principal directions, respectively. Based on above definitions, LT and ILD are homogeneous along the circumferential direction for both the NT and HT cases. In contrast, LT and ILD are heterogeneous along the radial direction for both NT and HT.

(a) ANOVA of the Normotension LT Data.					
Source	Sum Square Error	Degree of Freedom	Mean Square Error	F-Statistics	Prob > F
Blocks	27121.5	193	140.526	36.93	0
Rows	1849.2	546	3.387	0.89	0.9687
Errors	400946.3	105378	3.805		
Total	429917	106117			

(b) ANOVA of the 4-week Hypertension LT Data.					
Source	Sum Square Error	Degree of Freedom	Mean Square Error	F-Statistics	Prob > F
Blocks	39078.3	207	188.784	42.34	0
Rows	1616.1	344	4.698	1.05	0.2377
Errors	317531.4	71208	4.459		
Total	358225.8	71759			

(c) ANOVA of the Normotension ILD Data.					
Source	Sum Square Error	Degree of Freedom	Mean Square Error	F-Statistics	Prob > F
Blocks	1453516	193	7531.17	96.67	0
Rows	44104.2	637	69.24	0.89	0.9794
Errors	9578285.7	122941	77.91		
Total	11075905.9	123771			

(d) ANOVA of the 4-week Hypertension ILD Data.					
Source	Sum Square Error	Degree of Freedom	Mean Square Error	F-Statistics	Prob > F
Blocks	1189810.3	206	5775.92	87.87	0
Rows	20542.8	375	54.78	0.83	0.9916
Errors	5077828.7	77250	65.73		
Total	6288211.7	77831			

Furthermore, comparison of images from 5 NT and 21 HT thoracic aortas revealed the following two key results:

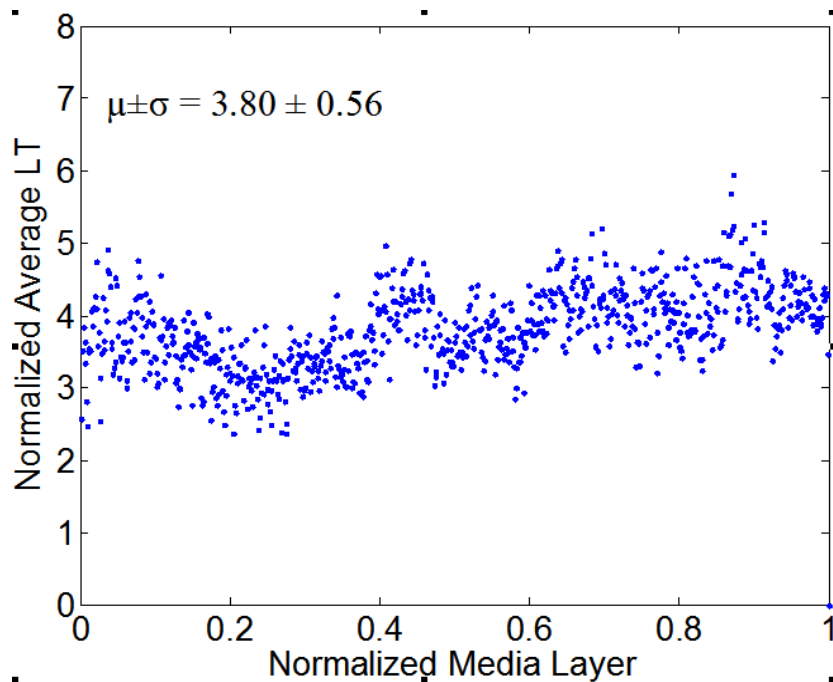
Result 1: LT and ILD exhibited regional heterogeneity along the radial direction for both NT and HT cases. All samples provided consistent F -statistics (close to 0) to support the heterogeneity hypothesis of LT and ILD distributions.

Result 2: LT and ILD exhibited regional homogeneity along the circumferential direction for both NT and HT cases. F -statistics of most samples were larger than $\alpha = 0.05$ (4/5 NT for LT and 3/5 NT for ILD, and 16/21 HT for LT and 18/21 HT for ILD). These results suggested that, in most cases, LT and ILD can be considered uniformly distributed along the circumferential direction under both NT and HT.

It is cautioned, however, that these results hold for the specific samples considered and should not be thought to be true for all loading conditions for all aortas or aortic segments in general. Nevertheless, despite my fundamentally different methods of analysis, my findings are consistent with those of [32], that is, LT is not uniformly distributed along the radial direction in general. As such, gross averages of point-wise measurements may fail to detect subtle changes of LT and ILD with time or location within the wall. The evaluation outcomes also validate the usefulness of the computer-based analysis scheme, hence it can be applied reliably to large scale studies.

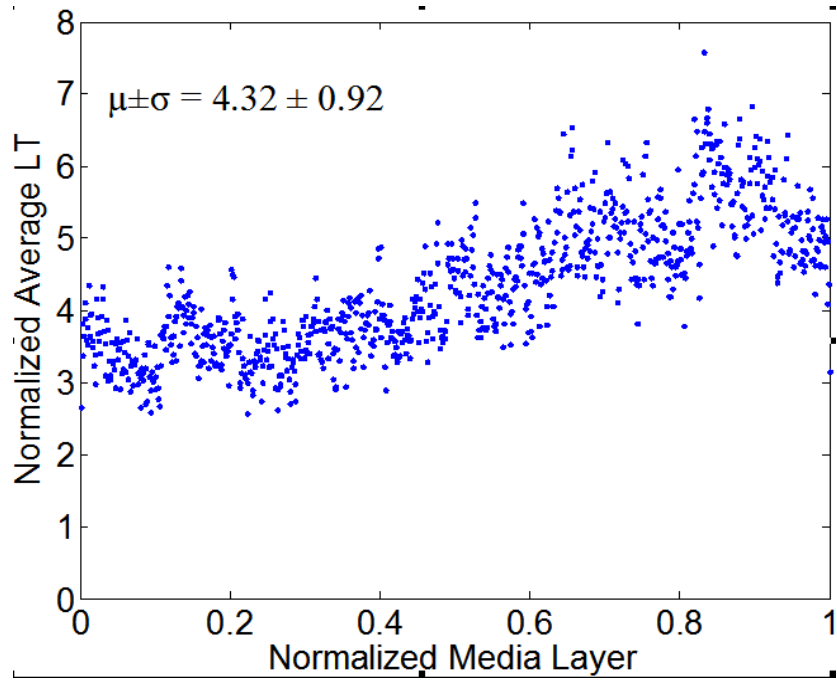
Figure 7 illustrates representative distributions of LT and ILD along the radial direction of a NT (Figure 7a) and a 4-week HT (Figure 7b) aorta sample, where the x -axis denotes a normalized media layer coordinate and the y -axis the averaged LT (with

the unit of measurement per pixel). All observations were normalized onto a [0,1] range to facilitate comparison between samples. Figure 7 (c) and (d) show the corresponding distributions of ILD from the same samples. Clearly, neither the LT nor the ILD distributions through the wall were uniform, consistent with the outcome of the hypothesis testing. The average LT was only slightly higher for the HT (= 4.32) than the NT (=3.81) aortas, but there was a tendency toward a higher value toward the lumen in the hypertensive cases (Figure 7b).

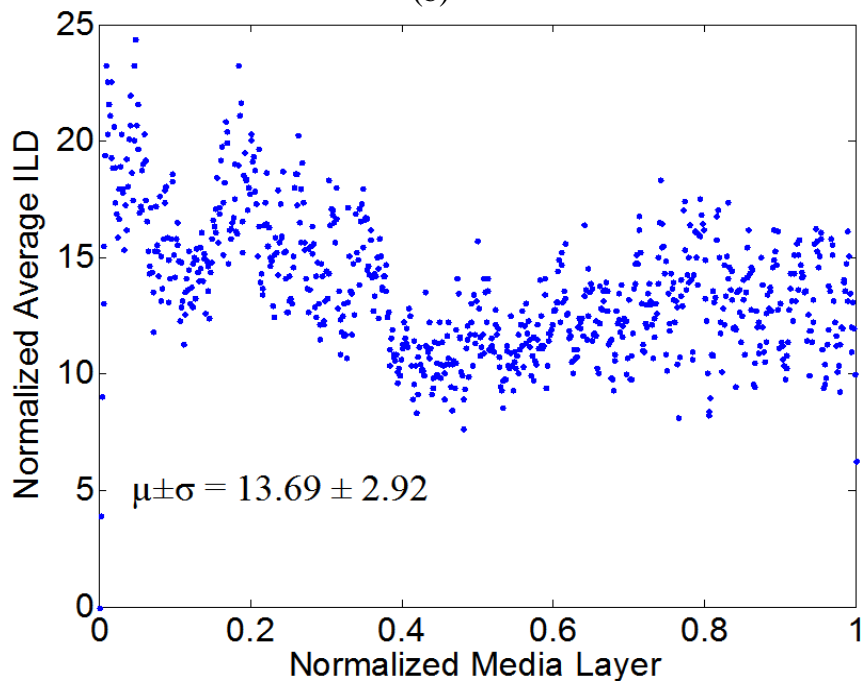


(a)

Figure 7. Computed elastic laminae thicknesses (a, b) and inter-lamellar distances (c, d) within the medial layers of representative normotensive (a,c) and 4-week hypertensive (b,d) thoracic aorta. Every point represents the average measurement within an analysis window for a fixed number of samples. Both the measurement locations (x-axis) and the measurements themselves (y-axis) were normalized to facilitate sample-to-sample comparisons; each data point is the result of the actual measurement divided by the maximum value of all measurements. The global mean and standard deviation of actual measurements are given at the bottom of each figure.

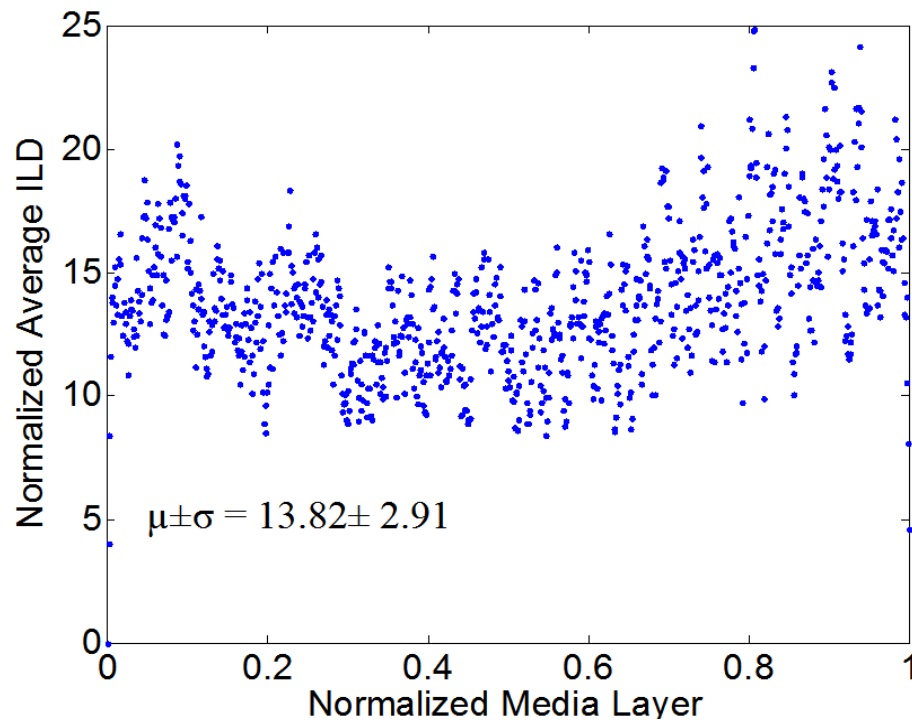


(b)



(c)

Figure 7. Continued



(d)

Figure 7. Continued

Various system indicators (or metrics) can be derived from the basic thickness maps for the elastic laminae. For instance, three different maps can be generated easily to visualize thickness patterns at a coarse level (Figure 8), where elastic laminae thickness LT is quantized into “below average” ($LT < \mu - \sigma$), “average” ($\mu - \sigma < LT < \mu + \sigma$), and “above average” ($LT > \mu + \sigma$). Visual inspection suggested that elastic laminae in the “below average” and “average” maps were fairly uniform whereas those in the above “average” map were less so. In other words, the non-uniform distribution of LT appeared to be due to those laminae having a greater thickness, particularly in hypertension.

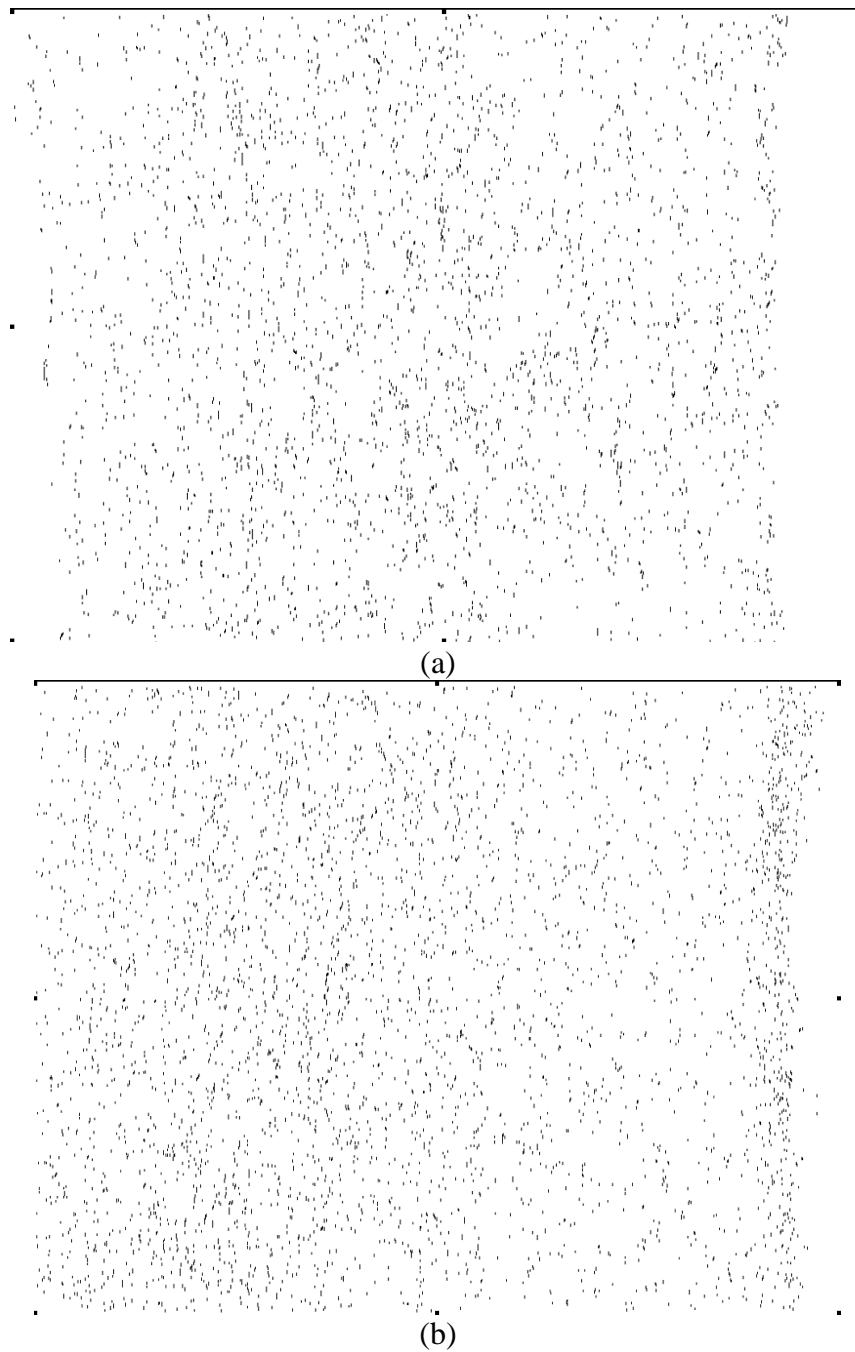
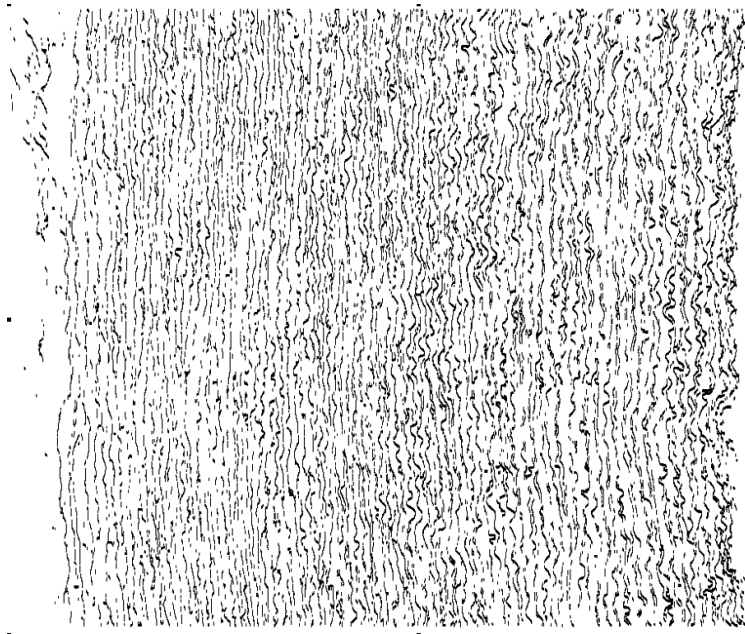
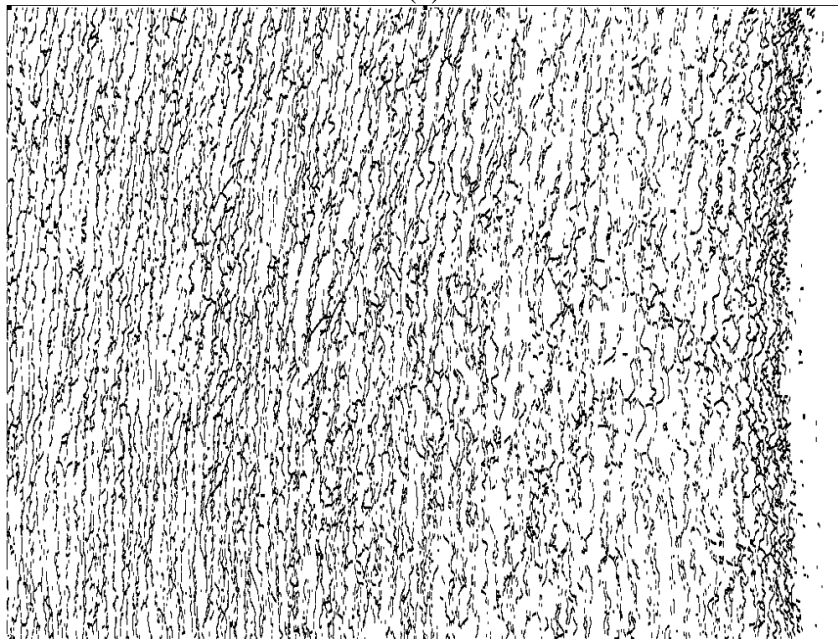


Figure 8. Regional, spatial non-uniformities of the laminae thickness (LT) illustrated by a simple thresholding routine: (a) and (b) below average ($LT < \mu - \sigma$), (c) and (d) average ($\mu - \sigma < LT < \mu + \sigma$), and (e) and (f) above average ($LT > \mu + \sigma$). In above figures, (a), (c) and (e) are outcomes of NT. (b), (d) and (f) are outcomes of HT.



(c)



(d)

Figure 8. Continued

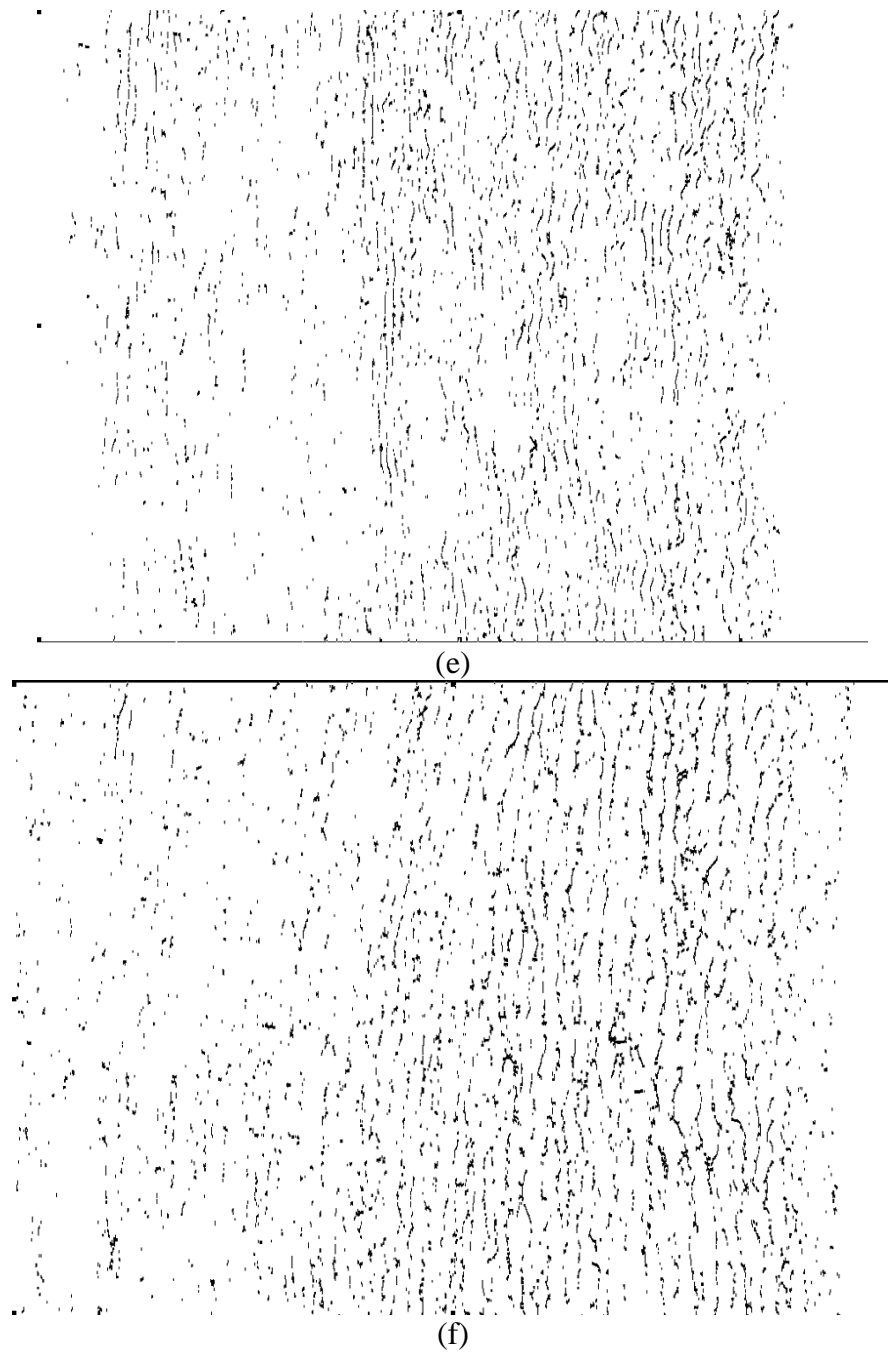


Figure 8. Continued

2.5 Aortic fragmentation measured via furcation point densities

A furcation point (FP) is a point at which an elastic lamina divides into two or more branches. The FP density could thus indicate fragmentation, or tearing, of elastic laminae under different conditions. Although general techniques for detecting vascular networks [33, 34] can be used for FP detection, they are not applicable for my needs. For example, the common practice of merging closely located bifurcation points (bi-FPs) would introduce significant errors, and modeling bi-FPs as a supremum of openings having a morphological T shape [33] would introduce significant artifacts. Rather, I followed the basic model of FP detection described in [33] and used matching of templates (see Figure 9) within 3x3 analysis windows on the elastic laminae skeletons to get my results.

By visual inspection, I found that the 22 templates defined in Figure 9a (note: the first two patterns have only one configuration, but the third to the seventh patterns have four orientations) were adequate for my needs, where a hollow circle is a skeleton pixel only, a gray circle is a skeleton pixel that cannot be a furcation point, and a solid black circle is a furcation point. Based on initial FP detection, as illustrated in Figure 9b, FP area density and line density were computed as:

$$\mu_{S,FP} = (1 / S_{CS}) \sum_{i=1}^n w_i , \quad (8)$$

$$\mu_{L,FP} = (1 / L_{EL}) \sum_{i=1}^n w_i , \quad (9)$$

where n is the total number of FPs within a designated analysis area.

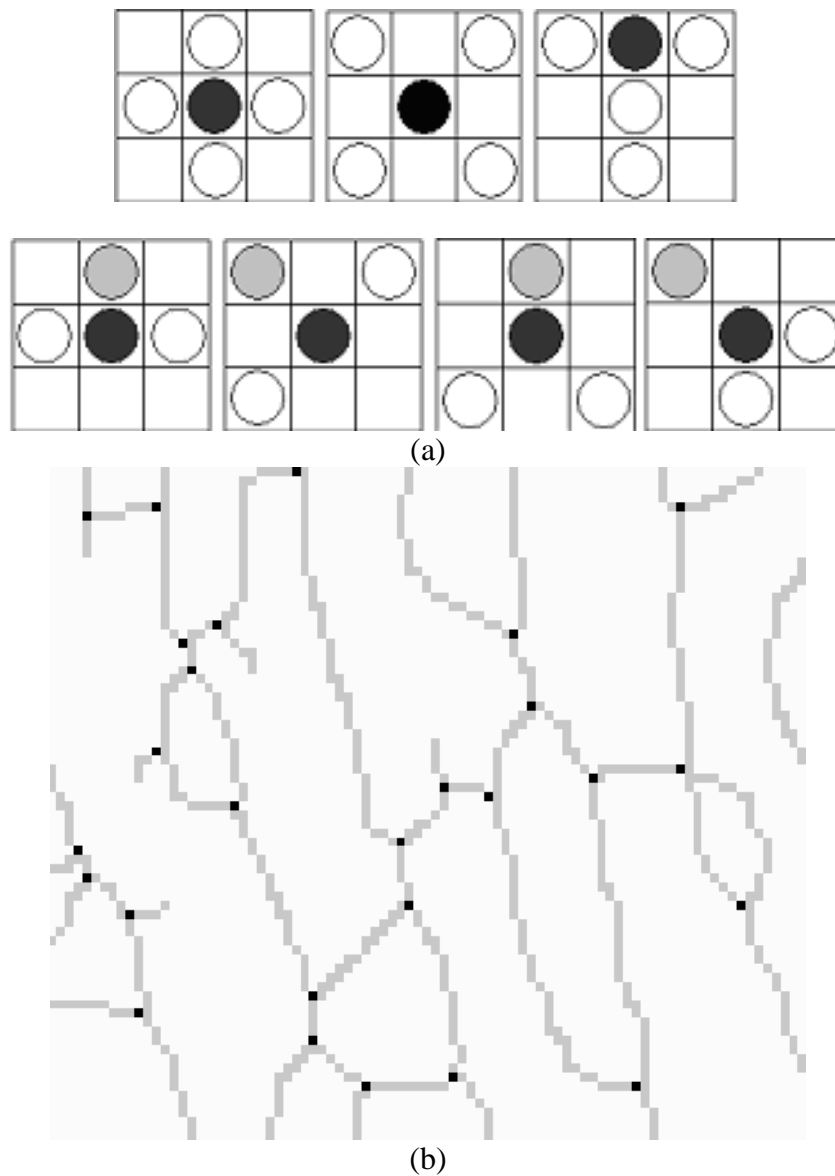


Figure 9. (a) Furcation Point (FP) Analysis using 22 standard templates (note: the first two patterns from the left allow one configuration each whereas the third to the seventh patterns allow four different orientation situations each). These templates were trained using sample images to locate furcation points, denoted by a black circle. A grey circle denotes a skeleton pixel not on a furcation point, and a hollow circle denotes a skeleton pixel. The block need not be considered if it does have any of the marks mentioned above. (b) Furcation points (marked in black dots) detected from skeleton lines (marked by light gray lines) for a representative magnified local section from an aortic image.

S_{CS} is the total analysis surface area, L_{EL} is the total length of elastic laminae within S_{CS} , and w_i is the weight of the i^{th} FP (the weight of a FP with $m+1$ branches is $m-1$, for example, a bi-FP has three branches and a weight of one). These two densities could be used to characterize elastin fragmentation or perhaps incompletely deposited fibrils under different conditions. Illustrative results are shown in Table 6 and Figure 10 for five classes of aortic samples: surgical controls (normotensive) and 2-, 4-, 6- and 8-week hypertensive (HT) samples. As it can be seen, the longer durations of hypertension resulted in larger differences in both FP metrics from control values, thus suggesting either greater fragmentation or perhaps the deposition of new elastic fibers that were not incorporated completely within extant laminae. Note that these differences are reflected by the changes Δ_S and Δ_L relative to the surgical controls (SC).

Table 6. Area and line density of furcation points corresponding to Figure 10.

	$\mu_{S,FP}$ (10-3)	N	Δ_S (%)	$\mu_{L,FP}$ (10-2)	N	Δ_L (%)
SC	2.62±0.26	17		3.98±0.15	14	
2-W	2.46±0.23	14	-5.86	4.03±0.30	17	1.44
4-W	2.53±0.28	13	-3.32	4.17±0.25	10	4.89
6-W	1.99±0.32	14	-23.87	3.62±0.34	15	-9.05
8-W	1.31±0.20	19	-49.93	3.3±0.24	16	-17.09

I list five groups of aorta in this table: surgery control (SC, which is normotensive), 2-week, 4-week, 6-week and 8-week hypertension (HT). The second and fifth columns are the FP area and line density measurements, average and standard deviation. The third and sixth columns are the sample image counts used in each group.

The fourth and seventh columns are differences relative to results for SC. I found μS , FP (furcation point area density) to decrease monotonically with the duration of HT and μL , FP (furcation point line density) to increase slightly at 2- and 4-weeks, and then decrease sharply.

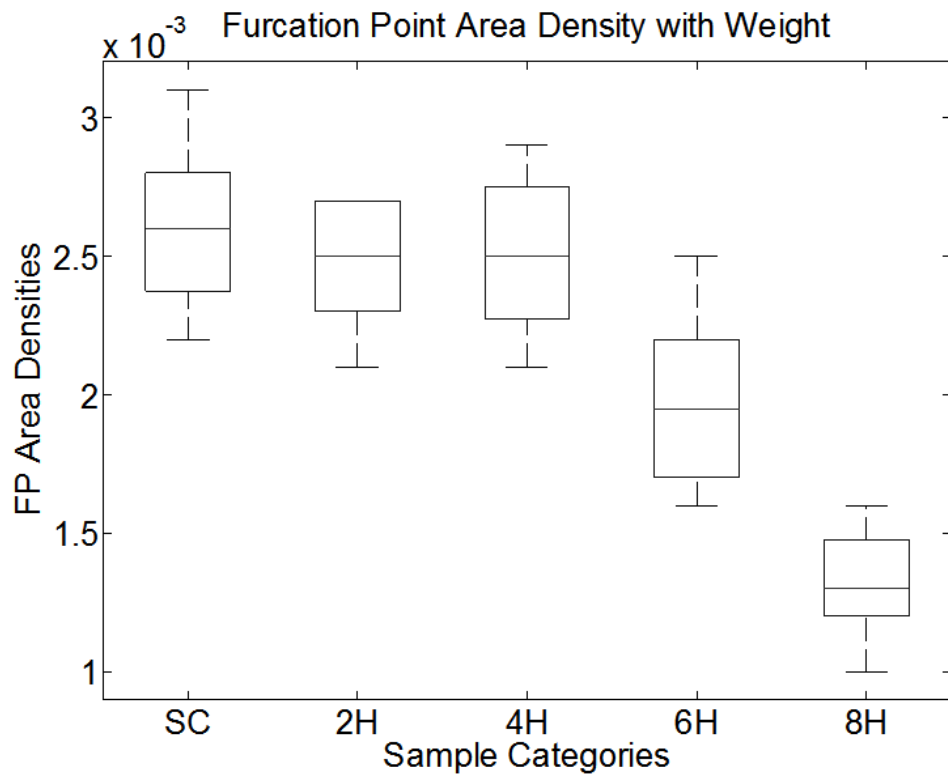


Figure 10. Furcation point area (line) density boxplots of data from Table 6. Both computations include five categories: surgery control (SC) and two-, four-, six- and eight-week HT aortic samples. X-axis shows the categories, y axis demonstrates the FP area (left) and line (right) densities. The middle line in each box is the median within each group. The upper and lower bound of each box is the lower (25%) and upper (75%) quartile.

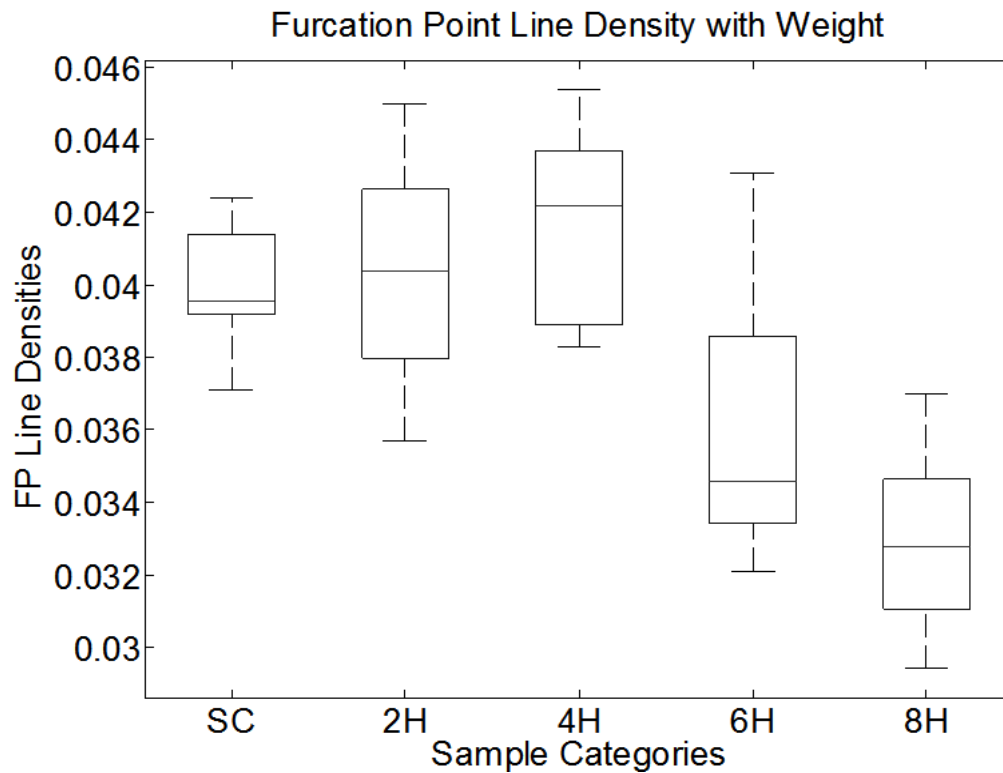


Figure 10. Continued

The FP area density distribution was relatively uniform under normotensive conditions (Figure 11a), but there was a spiked local increase and global elevation within the central region in hypertensive specimens (Figure 11b). It is not clear why there was more pressure-induced remodeling within the middle region of the media under hypertension while regions closer to intima and adventitia were less affected, but these are the types of observations that are needed to generate new hypotheses for the mechanobiology.

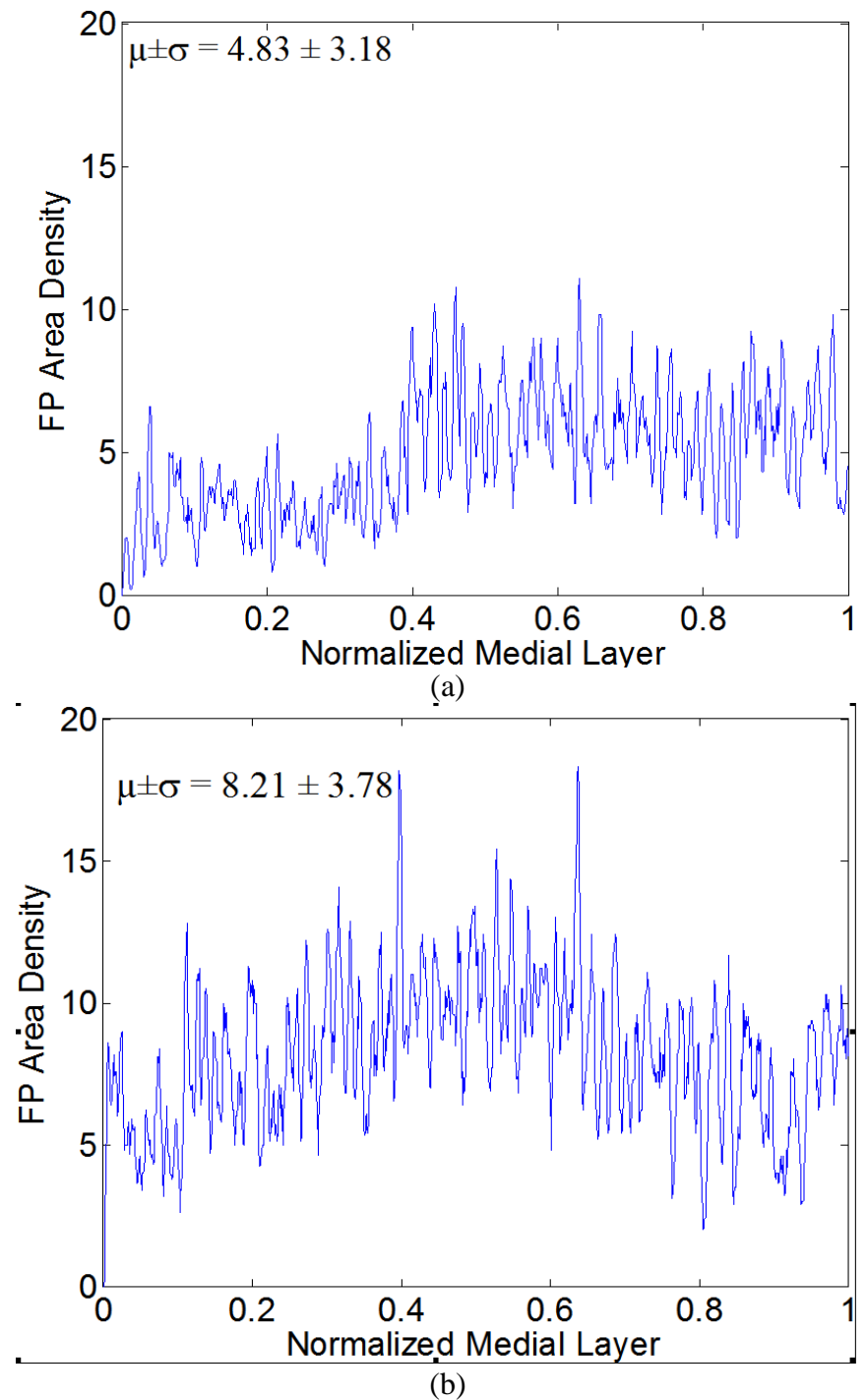


Figure 11. Furcation point (FP) area density measurements with a running average (window size is five) for representative (a) normotensive and (b) 4-week hypertensive samples. These results show a higher mean value of FP area density for the hypertensive sample, with a significant increase within the middle of the medial layer. Such measurements can be used to generate higher order statistics if desired.

Finally, although not shown, the mean length of elastic laminae was slightly greater in NT aortas near the outer (adventitial) layer, but uniform in other regions. In contrast, the elastic laminae were slightly longer in the central region in HT, but shorter in the region close to the intima. Average laminae length increased 6.6% from NT (=183.2 pixels) to 4-week HT (=195.3 pixels) while total length decreased by 35.5% from NT (=1746 pixels) to 4-week HT (=1127 pixels). In both conditions, maxima and minima occurred near the adventitia and intima, respectively. The area of the detected laminae also increased, by 11%, from NT (=717.0 pixels) to HT (=796.0 pixels), with maximum and minimum values occurring within the central region and near the intima, respectively.

CHAPTER III

VIRTUAL LAYER

3.1 Definition and purpose of virtual layer

The main goal of the VL model is to support cross-image study of morphological changes of select organelles in the format of a dense numerical matrix, which is aligned to the principle direction of ELs. In [27, 35], I have developed an RT-based algorithm to compute the principal direction of ELs and obtain LT and ILD measurements from ridge lines of ELs. Those point measurements form a sparse matrix, in which only locations of EL ridge lines contain non-null values. It is numerically difficult to analyze this matrix as is by naked eye or computing algorithms. Moreover, the wavy, sometimes twisted ELs of different lengths make it very difficult to define EL layers from inner to outer aorta walls. The VLM of the LT/ILD map is abstraction of measured points so that for LT (ILD) morphological analysis, only LT observations of each image need to be mapped to its corresponding VLM. Columns of VLMs are aligned to principal directions of ELs, and all images are mapped to their VLMs of a same dimension. Interpolation of adjacent observation points in the original image onto its VLM also serves as a simple smoothing technique to reduce effects of local spikes. This way, noise (short EL branches) can be removed during the mapping process, and layer to layer morphological analysis can be done with much simplified computing algorithms.

In my earlier work [27, 35], I have successfully used Radon transform to map ELs and their principal directions. To further reduce the number of calibration

parameters required for analysis, and to improve robustness against noise, in this work I develop a novel technique based on the Log-Gabor Filter (LGF) [36-42] and an adaptive search algorithm. At the first step, the image is filtered by LGF to generate a pixel level orientation map. Then, I apply the adaptive threshold- morphological thinning technique proposed in [24] to extract EL ridge lines from the original image. Ridge lines obtained from this step contain many minute branches due to imaging artifacts, cutting, etc. To eliminate high frequency noise, I develop an automated search routine to detect larger branches, using pixels with largest LT measurements as starting points. Using orientations of LGF values as inputs, the greedy search routine [43] searches for the best direction of the EL ridge pixel by pixel, until it meets termination conditions.

Let the VLM of EL ridge map be denoted as an $n \times m$ dense matrix. Typically, the height of a ridge map ranges from 1000 to 2000, and there are 50 to 60 major EL ridge lines. Many branches and furcation points may concentrate on a small area. It has been shown earlier [27, 35] that, the EL thickness remains fairly constant along the principle direction of EL. As a result, for most cases I set $n=m=256$, so that all branches can be accounted for, and the square structure of VL makes it easier for numerical computations and analysis. Specific steps to map a ridge map of EL image to its VL representation are outlined as follows:

- (1) Rotate the orientation of the ridge line map to align the principle direction of ridge lines [27, 35] vertically. The rotated image is reduced to n rows in two steps. In the first step, top and bottom rows are trimmed until no row contains

null pixels (due to rotation). In the second step, non-null LT/ILD values on each row are linearly interpolated into m points onto the VLM.

- (2) The number of rows of the VL matrix is downsized from n to 256. This step helps smoothing minor local variations along the principle direction.

Main computing steps required for automated generation of VLM are summarized in Figure 12. The example given in Figure 2 demonstrates the relationship between an original aorta image (Figure 13(a)), its EL and EL-ridge maps (Figure 13 (b) and (c)), and its VLM (Figure 13 (d)). This figure contains only a small fraction of an aorta image is used for better illustration of the mapping effects. Otherwise, a full aorta image would contain much more EL layers, making it difficult to visualize morphological structures of ELs. In Figure 13 (b), cross marks in green color represent automatically generated starting points for an EL ridge line search scheme.

The VLM provides a smoothed representation of discrete LT/ILD points through the re-sampling and interpolation processes. An immediate benefit of VLM is clear visualization of localized LT/ILD regions or clusters, which would be otherwise very difficult to observe on the original image. One can apply/design automated segmentation/classification techniques for single-modal (LT or ILD alone) and modal-correlated studies. My experiments show that statistics derived from VLM-based analysis are consistent with those derived from the EL map of a morphological thinning method [35]. The key differences are that (1) the VLM based method is more robust to noise, and (2) the VLM technique is much more effective in eliminating artifacts

introduced by minute EL branches. Details on design and robustness evaluation of the log-Gabor filter and EL search algorithm are discussed in the next two subsections.

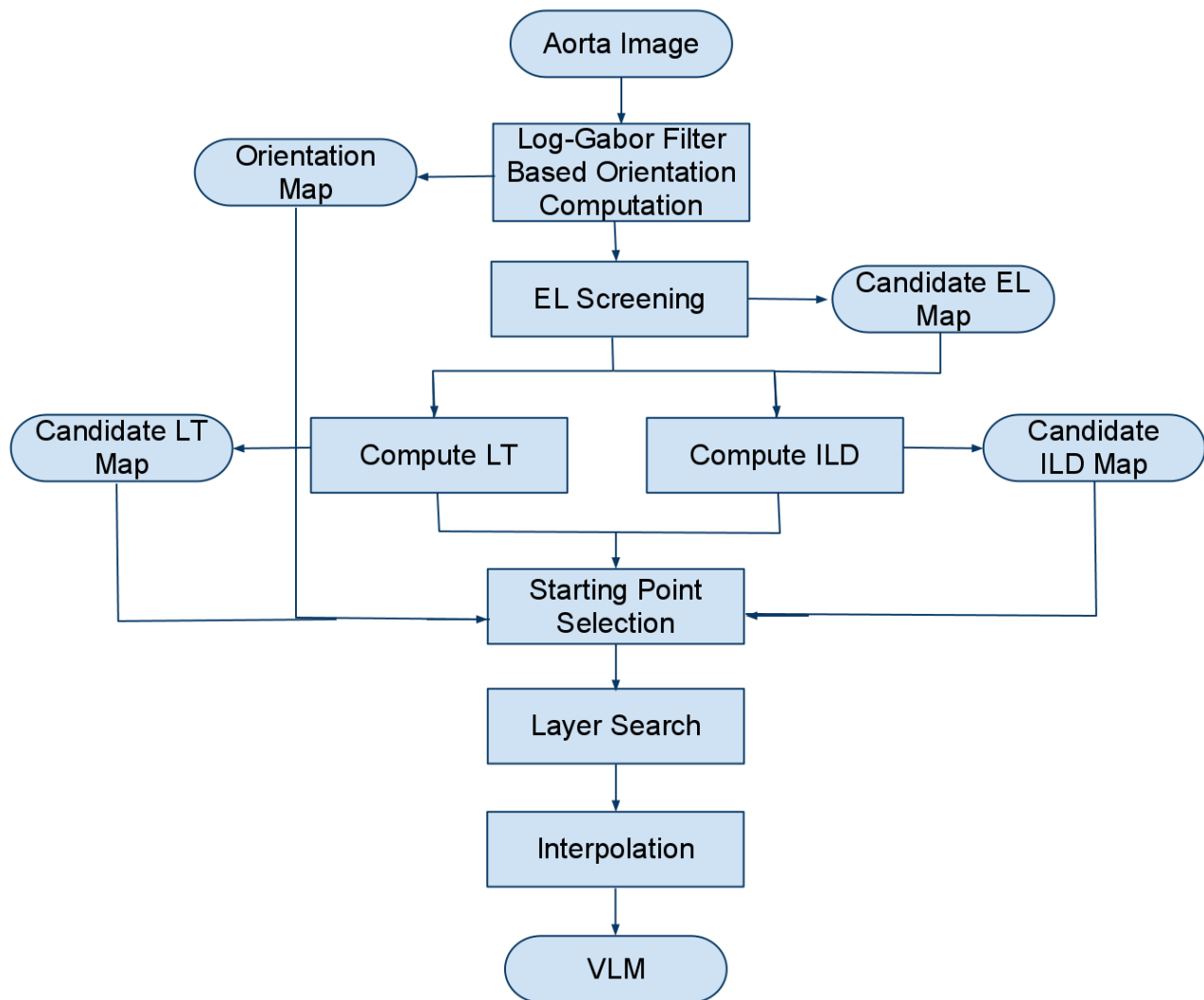
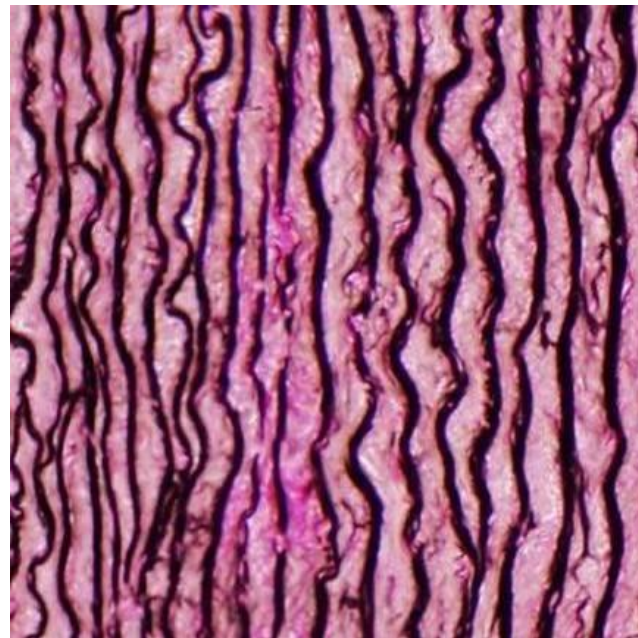
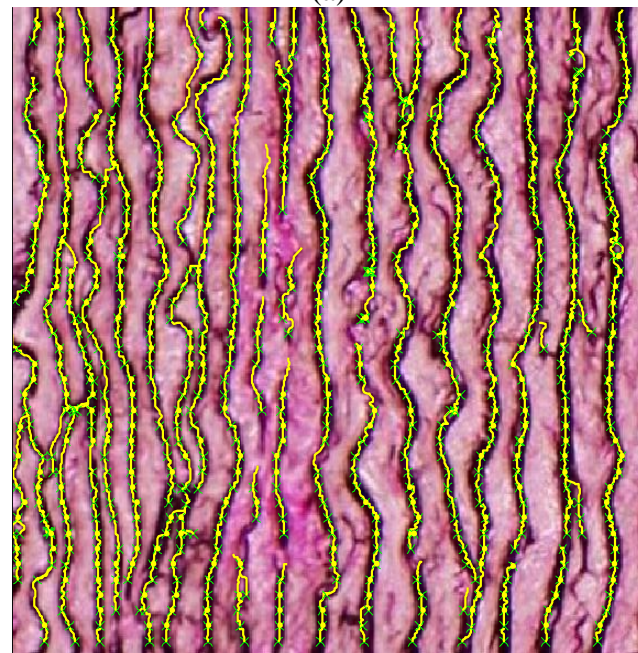


Figure 12. Computing steps for automated generation of VLM for an aorta image.

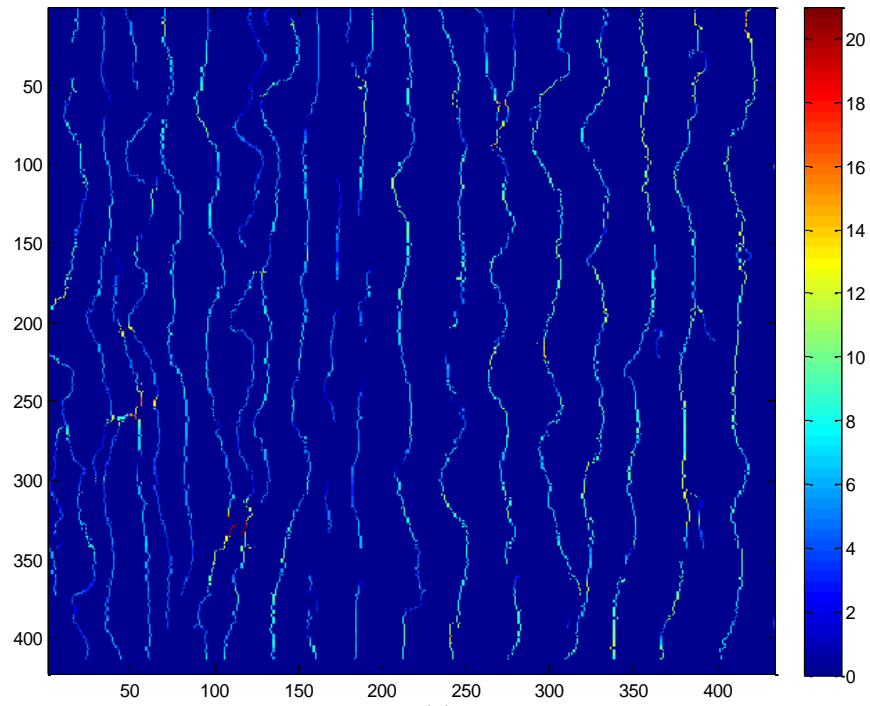


(a)

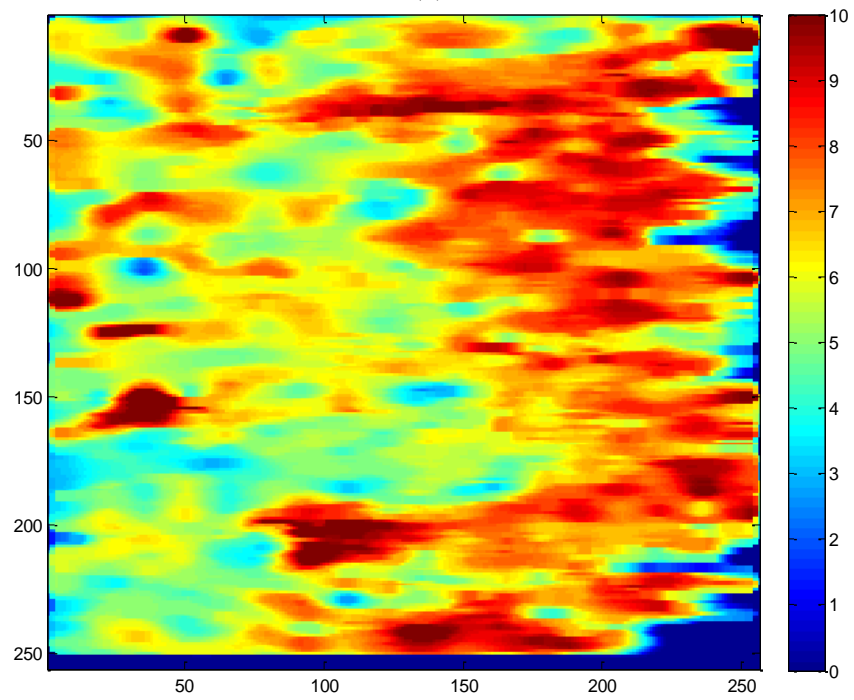


(b)

Figure 13. (a) An aorta image. In this image, ELs on the left side are thinner than those on the right side. (b) Automatically generated starting points (cross marks in green), and ELs (yellow lines). (c) Color coded LT map for LT values on EL ridge lines. d) The VLM of the LT map.



(c)



(d)

Figure 13. Continued

3.2 Log-Gabor filter

Log-Gabor filter [40, 44] is essentially a logarithmic transformation of Gabor Filter, which is able to eliminate the DC-components in frequency domain. It is widely used for detection of orientation of patterns. The Log-Gabor filter can be expressed as follows:

$$G(w) = \exp\left[-(\log(w/w_0))^2/2(\log(k/w_0))^2\right], \quad (10)$$

where w_0 is the center frequency of the filter, w is the frequency and k is a constant value. In this dissertation, a generalized Log-Gabor filter was applied to obtain the orientation of each pixel within the EL. An example and its enlarged outcome are in Figure 14. The

A major advantage of LGF is its robustness against noise. In the following Figure 15, Gaussian noise was applied to two images with different variances. It is obvious that the LGF based algorithm is able to detect the EL directions correctly even with strong noises.

Based on the orientation calculated, I can decide how EL goes based on one predefined rules: EL always goes within $\pm\pi/2$ degree range. It restricts that the orientation differences of neighboring two pixels will not larger than π .

In the following image, I provided some seeking results. The top image is the original image. The bottom is the image processed with median filter. On the bottom, with each click, my algorithm will automatically seek a thread of EL based on the calculated orientation. It is easy to observe that the result is very accurate and the furcation point will not be a problem. To avoid of repetitive labeling (a part of EL thread was labeled twice), I define that: an EL can only be labeled once.

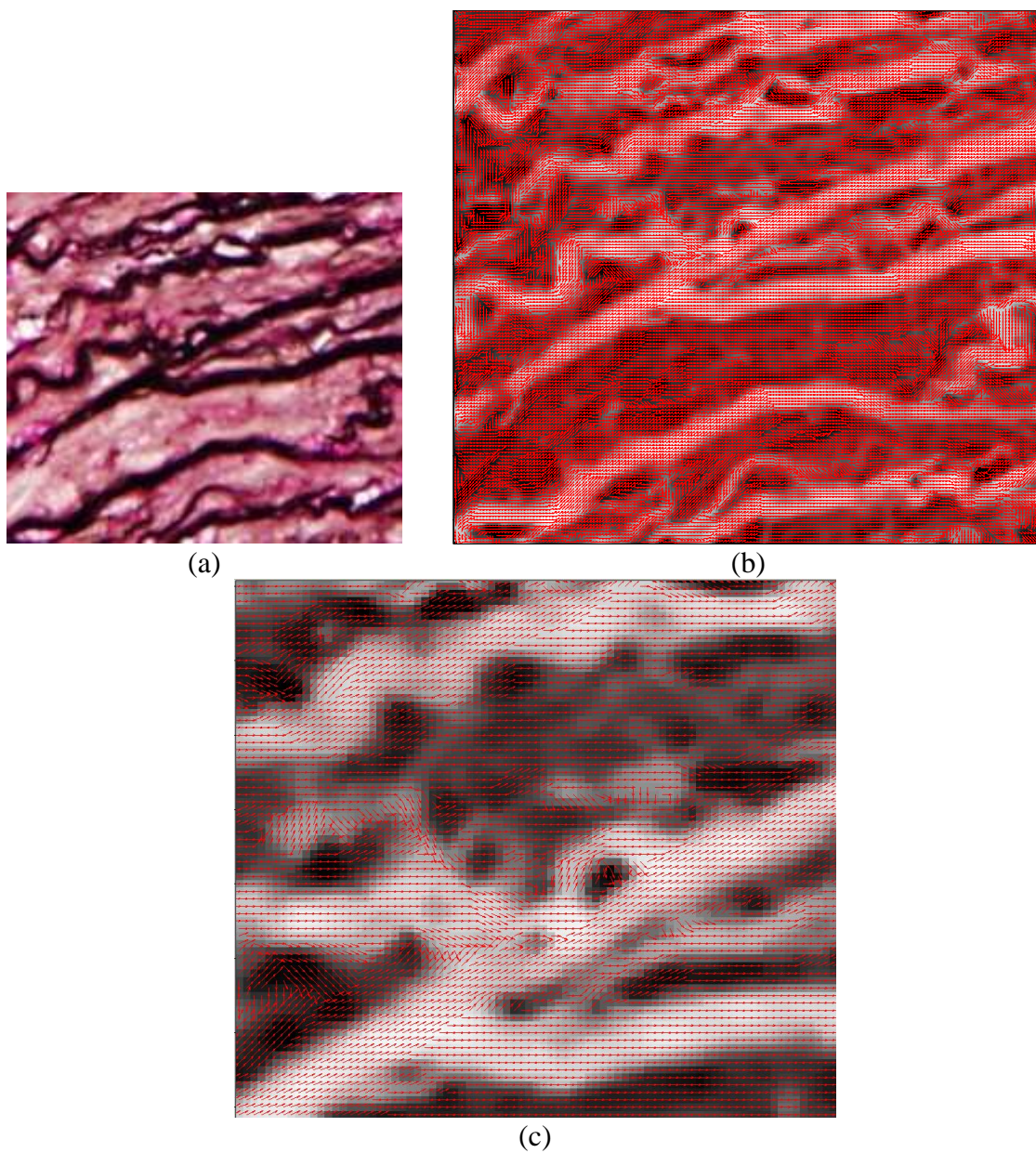


Figure 14. (a) An original image, on which white regions represent EL, and black regions for smooth muscle cells and collagen. (b) The Log-Gabor map of the image. (c) a zoom-in view of a cropped area of (b). Red arrows show the local tissue orientation computed through LGF. If the local orientation is zero, it will show as one red dot.

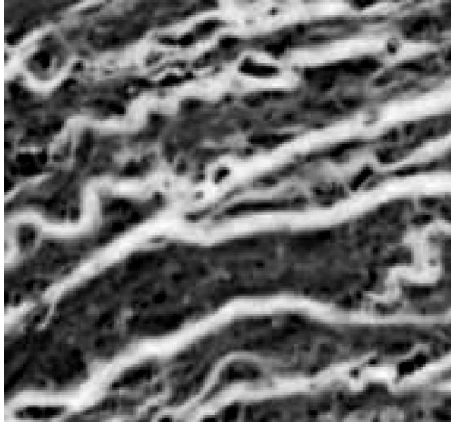

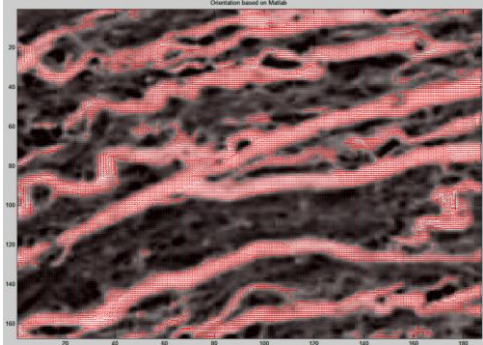
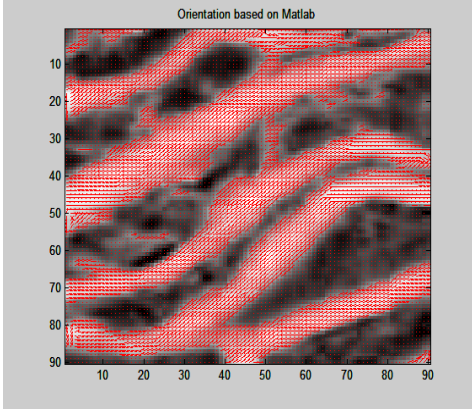
Parameters	Sample Image 1	Sample Image 2
Original	 <p style="text-align: center;">(a)</p>	 <p style="text-align: center;">(a')</p>
Orientation Map	 <p style="text-align: center;">(b)</p>	 <p style="text-align: center;">(b')</p>

Figure 15. LGF based algorithm is robust to noises. (a) and (a') are two different aorta cropping. (b) and (b') are the orientation map. For a better visual effect, in (b) and (b'), only the directions on the ELs are shown in the figure. In (c),(c'), (e) and (e'), Gaussian noises with $\sigma = 0.1$ and 0.5 were applied to (a) and (a'). (d), (d'), (f) and (f') are their orientation map respectively.

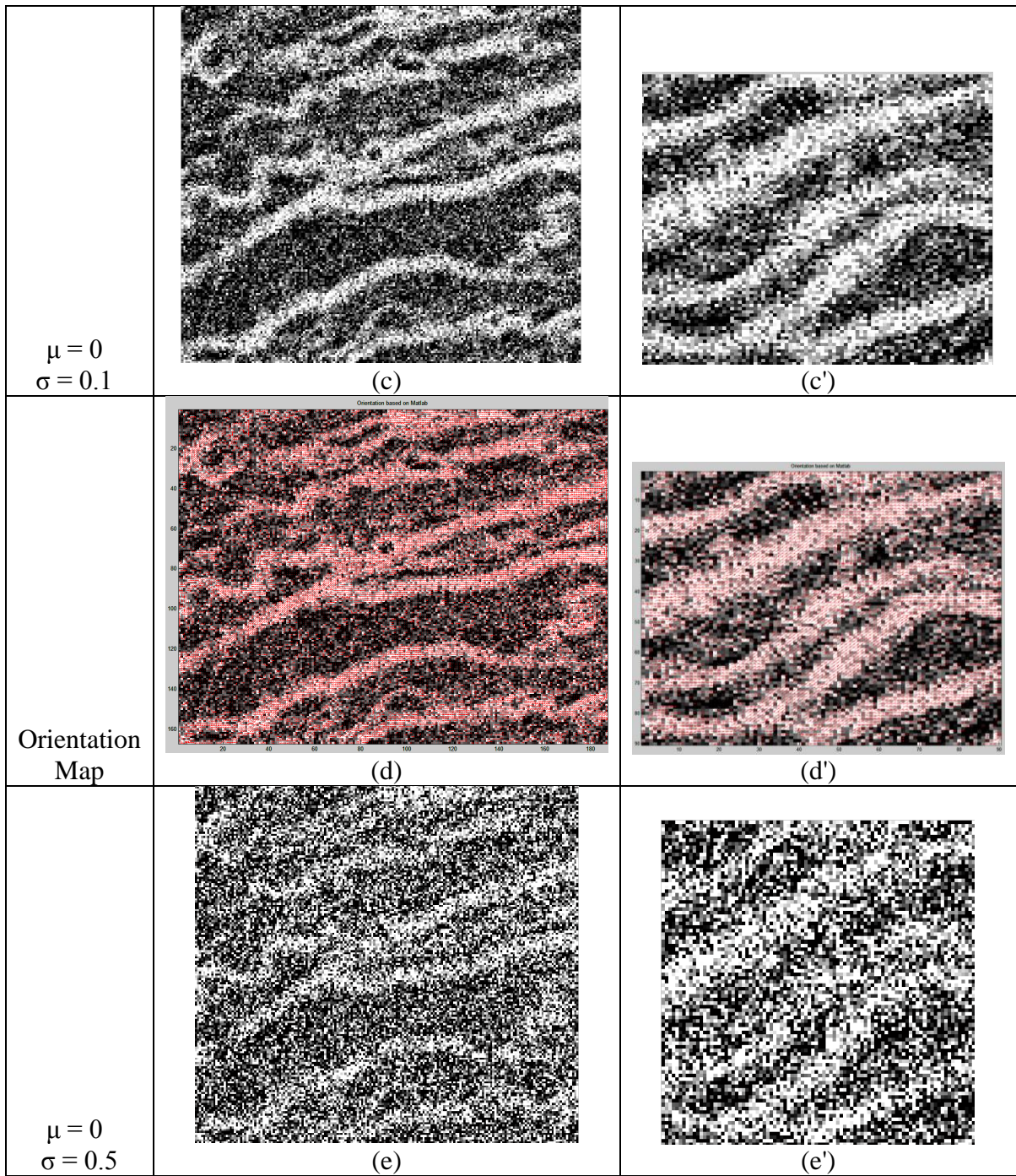


Figure 15. Continued

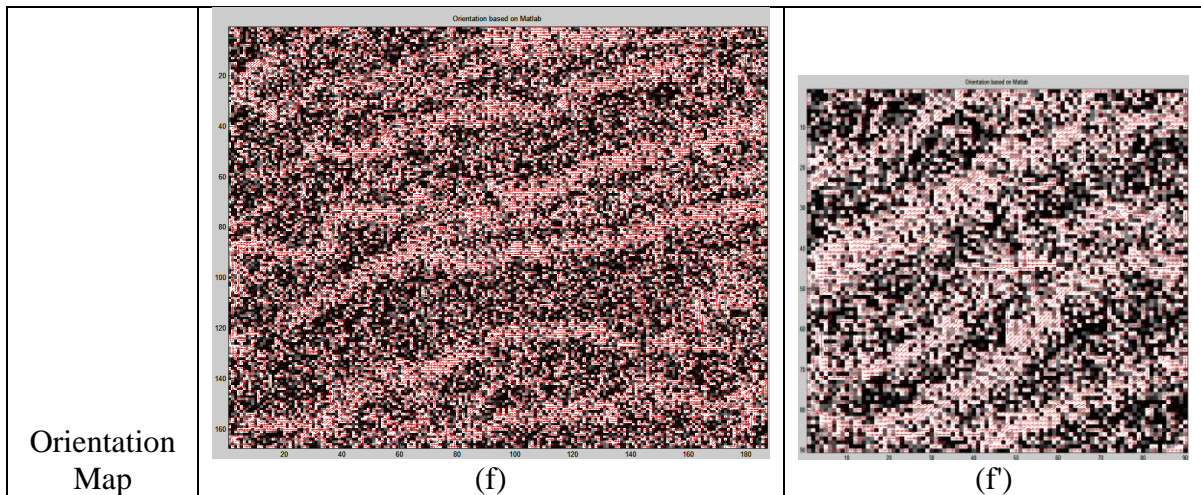


Figure 15. Continued

3.3 Comparison between Gabor and Log-Gabor filters

There are many other frequency domain filter based algorithms, Gabor filter is another choice. In the pattern recognition and image processing, Gabor filter is widely applied in edge detection, feature extraction and specified pattern recognition [45, 46]. Frequency and orientation representations of Gabor filter are similar to those of human visual system, and it has been found to be particularly appropriate for texture representation and discrimination. In the spatial domain, a 2D Gabor filter is a Gaussian kernel function modulated by a sinusoidal plane wave. The Gabor filters are self-similar – all filters can be generated from one parent wavelet by dilation and rotation.

Its impulse response is defined by a harmonic function multiplied by a Gaussian function. Because of the multiplication-convolution property (Convolution theorem), the Fourier transform of a Gabor filter's impulse response is the convolution of the Fourier transform of the harmonic function and the Fourier transform of the Gaussian function.

To process images with clear patterns, such as the aorta lamina network structures, Gabor filter is not able to provide arbitrary bandwidth with a low DC component. This difficulty might make Gabor filter be prone to noises. I might have to apply multiple Gabor filters to maintain a wide coverage of the spectrum which is inconvenient.

$$g(x, y; \lambda, \theta, \psi, \sigma, \gamma) = \exp\left(-\frac{x'^2 + \gamma^2 y'^2}{2\sigma^2}\right) \cos\left(2\pi \frac{x'}{\lambda} + \psi\right), \quad (11)$$

where $x' = x \cos \theta + y \sin \theta$, $y' = -x \sin \theta + y \cos \theta$, λ is the wavelength of the cosine factor, θ is the orientation of the normal to the parallel stripes of a Gabor function, ψ is the phase offset, σ is the standard deviation of the Gaussian function and γ is the spatial aspect ratio.

To overcome this limitation, I chose Log-Gabor filter instead. The difference between Log-Gabor and Gabor filter is: Gabor filter has Gaussian transfer functions, but Log-Gabor filter [40] has a logarithmic frequency scale based kernel function.

To compare the laminae direction computation results based on above two algorithms, directions overlapping original image was provided in Figure 16. In the highlighted yellow ellipse, the direction computed by Log-Gabor filter is smoother than Gabor filter. In the other area, the Log-Gabor filter can provide the same accuracy as Gabor filter. The disadvantage of Log-Gabor filter is computation burden because Log-Gabor need to make calculation in frequency domain. FFT and IFFT will be called in each given direction to compute the energy. But Gabor filter only needs exponential function calculation which will be much faster.

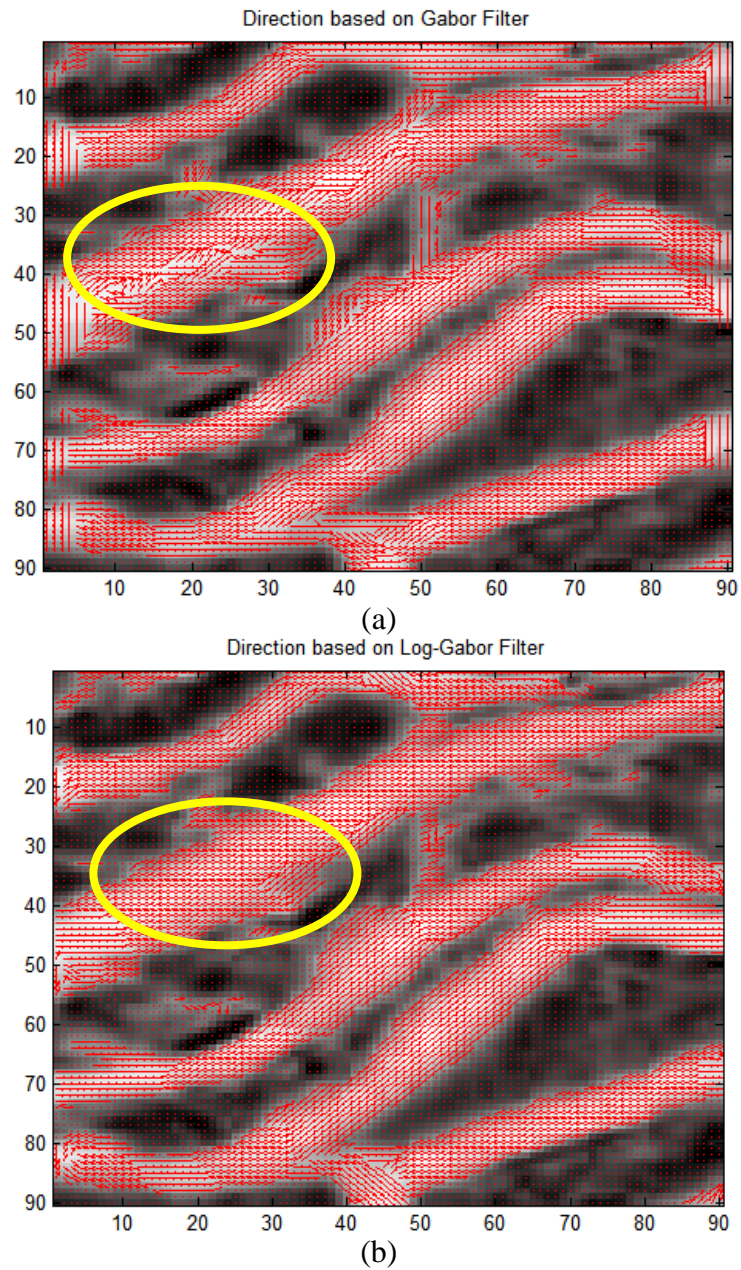


Figure 16. EL flow direction detection results by (a) Gabor filter, and (b) Log-Gabor filter. The original image was blurred and superimposed with the detection maps to highlight detection details, and red small arrow at each pixel points to the detected EL flow direction. A yellow ellipse highlights one of many regions in which the Log-Gabor filter produces significantly better consistency of detected EL directions than the Gabor filter.

3.4 Searching mechanism definition of EL

3.4.1 Searching criteria definition

After getting the orientation with LGF, in this section, I will briefly explain how to identify the EL automatically with a local greedy search algorithm. To identify all pixels upon a lamina, there are three requirements: initial point (IP), orientations and stopping criteria. First of all, an initial point (IP) locating at (x,y) is selected on the EL. Then based on the orientation θ at (x,y) (from LGF), the next identified pixel $P'(x',y')$ on the EL can be calculated as:

$$\begin{aligned}x' &= x + \Delta \\y' &= y + \tan\theta\end{aligned}\tag{12}$$

where Δ is a user defined searching step (in this dissertation, $\Delta=1$).

Next, the stopping criteria will be applied to each candidate pixel to guarantee they are on the EL. Finally, by repeating this processing, all pixels upon an EL thread will be identified. An searching algorithm outcome is illustrated in Figure 17.

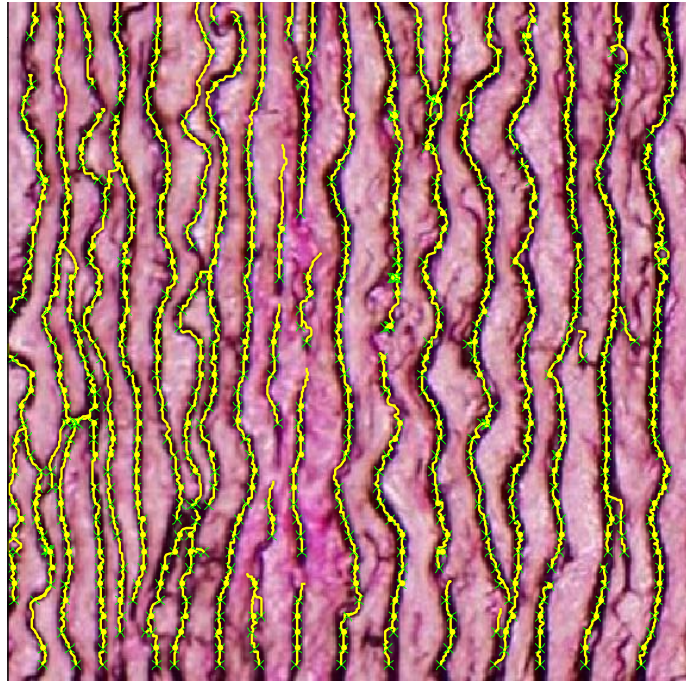


Figure 17. Aorta image with searched ELs highlighted with yellow

3.4.2 Aggregation of multiple search routes

When I applying the Log-Gabor searching algorithm, I found might be a multi-route problem: with one starting points, the searching result is the same without any problem. But if there is a small distortion of the initial point, the result might be far beyond the same, as Figure 18.

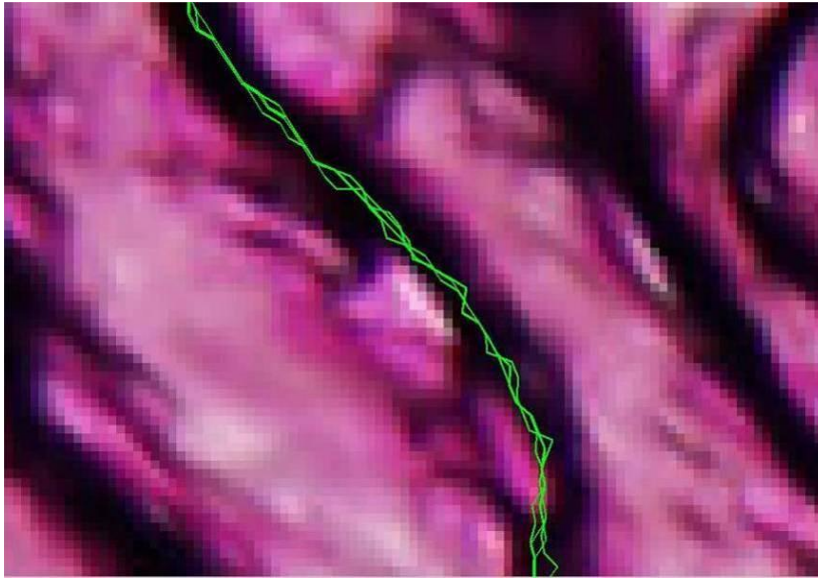


Figure 18. Multi-route issue: when searching the EL skeleton, based on different starting points, the searching results might be different. Then I might have a multi-route problem. In above figure, three routes were not completely overlapped.

The reason of this problem is the searching strategy. For a searching candidate point p , an analysis sampling window w with size h will be generated along the perpendicular direction of p . In w , the pixels with the largest intensity will be treated as the next pixel on the searching route. The problem of this strategy is:

1. If h is too large, the pixel with the largest intensity might be too far away from the center of the EL.
2. Normally, the intensities of the pixels in w illustrate a Gaussian-like distribution. But if there are multi peaks in w , different starting points might lead us to different searching routes.

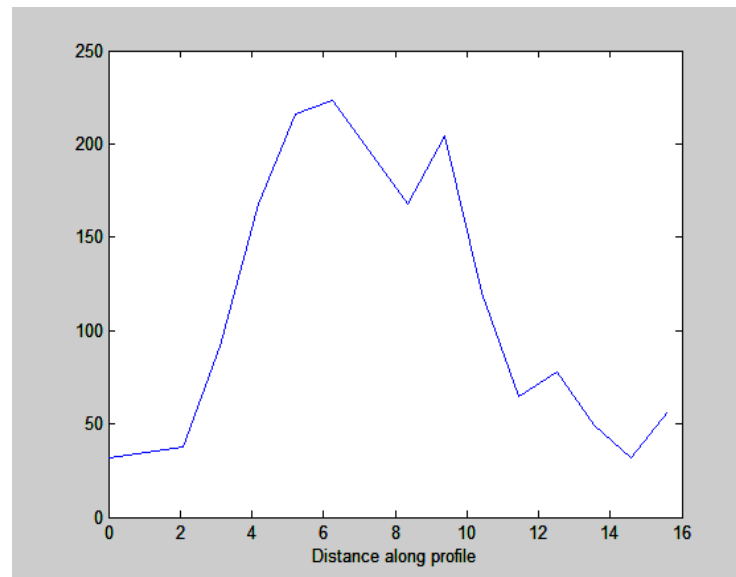
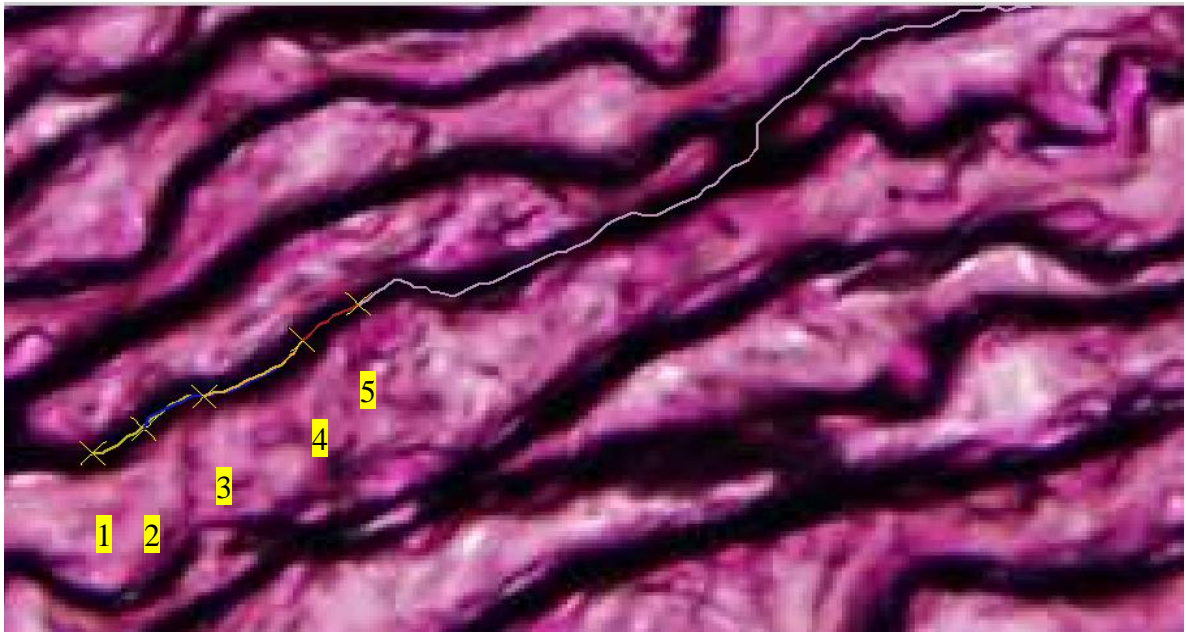


Figure 19. Simulation of pixel intensities within an analysis window. The intensity distribution distributes similar to a Gaussian. But multi peak phenomenon might happen.

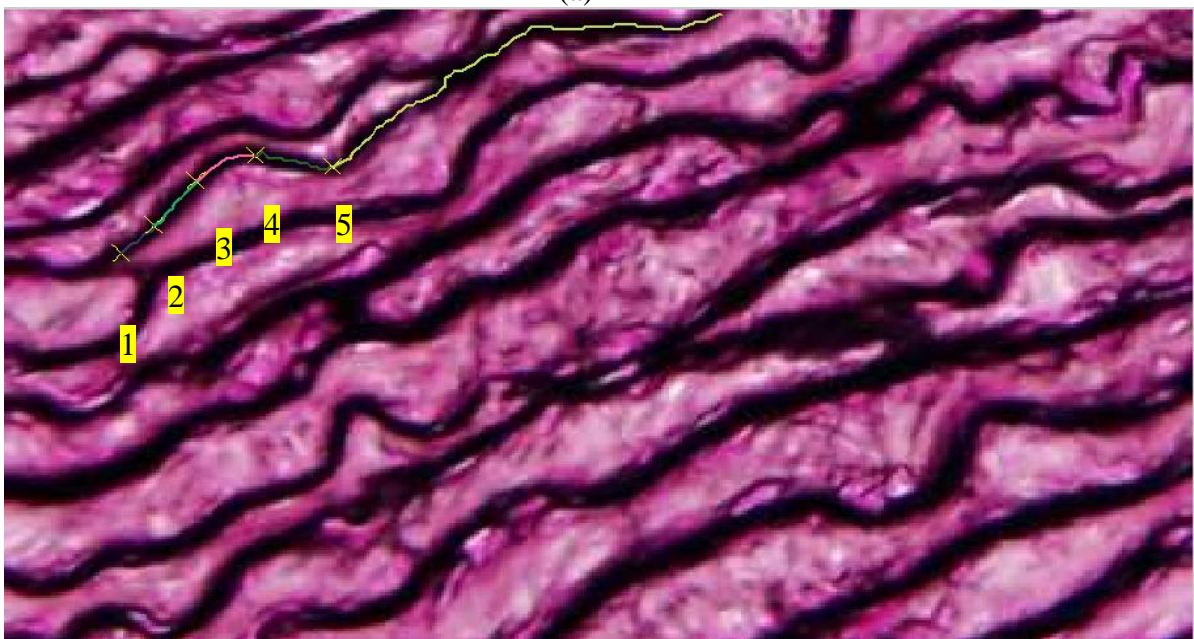
To overcome this issue, I revise the searching strategy by:

1. As the EL intensity is Gaussian-like distribution (Figure 19) along the intersecting direction, I applied Gaussian high-pass filter to remove the high-frequency noises.
2. Rather than searching the largest intensity pixel as a good pick, I start from previous candidate pixel. The closest peak to the candidate pixel will be treated as the next points on the route.
3. A stop criterion was set. When there is too much deviation of the current candidate from the previous point, then the searching process will stop to avoid of providing wrong result.
4. The searching window is set to be smaller to avoid of introducing noises.

Then the EL searching outcome will not have multi-route issue, shown in Figure 20.



(a)



(b)

Figure 20. Multi-route issue solution: in above figures (a) and (b), five different starting points are randomly and sequentially selected. They were marked as yellow crossing. The searching routes were highlighted with different colors. In (a), tracing results based on the five different starting points are not overlapped. After applying three more searching criteria, all these five starting points will have a completely overlapped route in (b).

3.5 Virtual layer segmentation

In my previous section, VLM visually illustrates some localized significantly thickened pattern, shown in Figure 13(d). In order to quantitatively classify this phenomenon, I applied k -means algorithm to segment the VLM into k regions (in this work, I choose $k = 3$).

k -means is a widely known iterative segmentation algorithm [47] which is applied to partition n observations $x = \{x_1, x_2, \dots, x_n\}$ into k (normally, $k \ll n$) presumed segments S . The purpose of k -means is to minimize the criterion function J , shown in (3), from the observation to its assigned centroid. Function J measures how well the observation set x is represented by the cluster centroids $\mu = \{\mu_1, \mu_2, \dots, \mu_k\}$. k -means algorithm includes three major steps:

1. Initialization: randomly or heuristically assign the n observations to k segments.
2. Update the assignment based on criterion function J .
3. Reassign n observations into k presumed segments.

After initialization, step two and three will be iteratively applied until all observation assignments do not change. In this work, conventional Euclidean distance was chosen to be the criterion.

$$J = \sum_{i=1}^k \sum_{x_j \in S_i} |x_j - \mu_i|^2 \quad (13)$$

where $\mu_i = \frac{1}{N_i} \sum_{x_j \in S_i} x_j$, N_i is the number of observations within segment S_i .

To implement k -means algorithm, first of all, cluster number need to be pre-defined which might be a challenge task. For simplicity, I am interested with three

layers: thickened, thinner and close-to-average regions. Thereafter, the number of clusters will be defined to be three.

To illustration the segmentation outcomes, shown in Figure 21 (d) and (f), I applied k -means technique to the VLM of one NT and one HT aorta sample images.

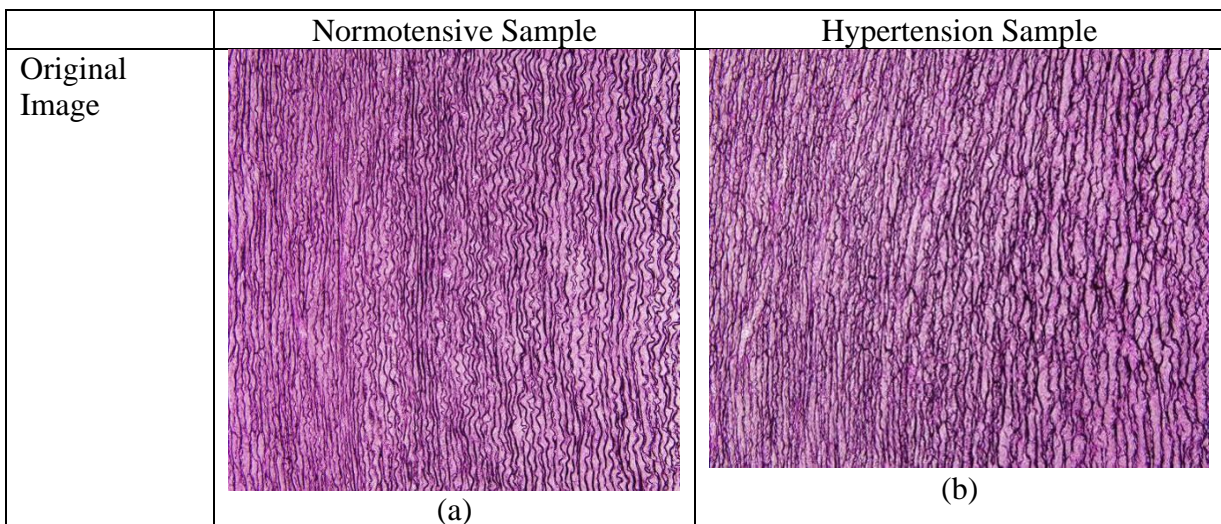


Figure 21. Porcine aorta LT morphology differences highlighted with k -means segmentation outcomes from VLM. (a) is a NT image, (b) is a HT sample, (c) and (d) are the generated VLM with Matlab pseudo color. Red represents high-value thickness and blue represents low-value. Green is a value in-between. (e) and (f) are the segmentation outcomes from k -means technique with three clusters pre-defined. Red color highlights the significantly thickened region. (g) and (h) are the outcomes by applying morphology operations (dilatation and removal) to smooth the segmentation outcomes. (i) and (j) are the smoothed segmentation outcome imposed over original images.

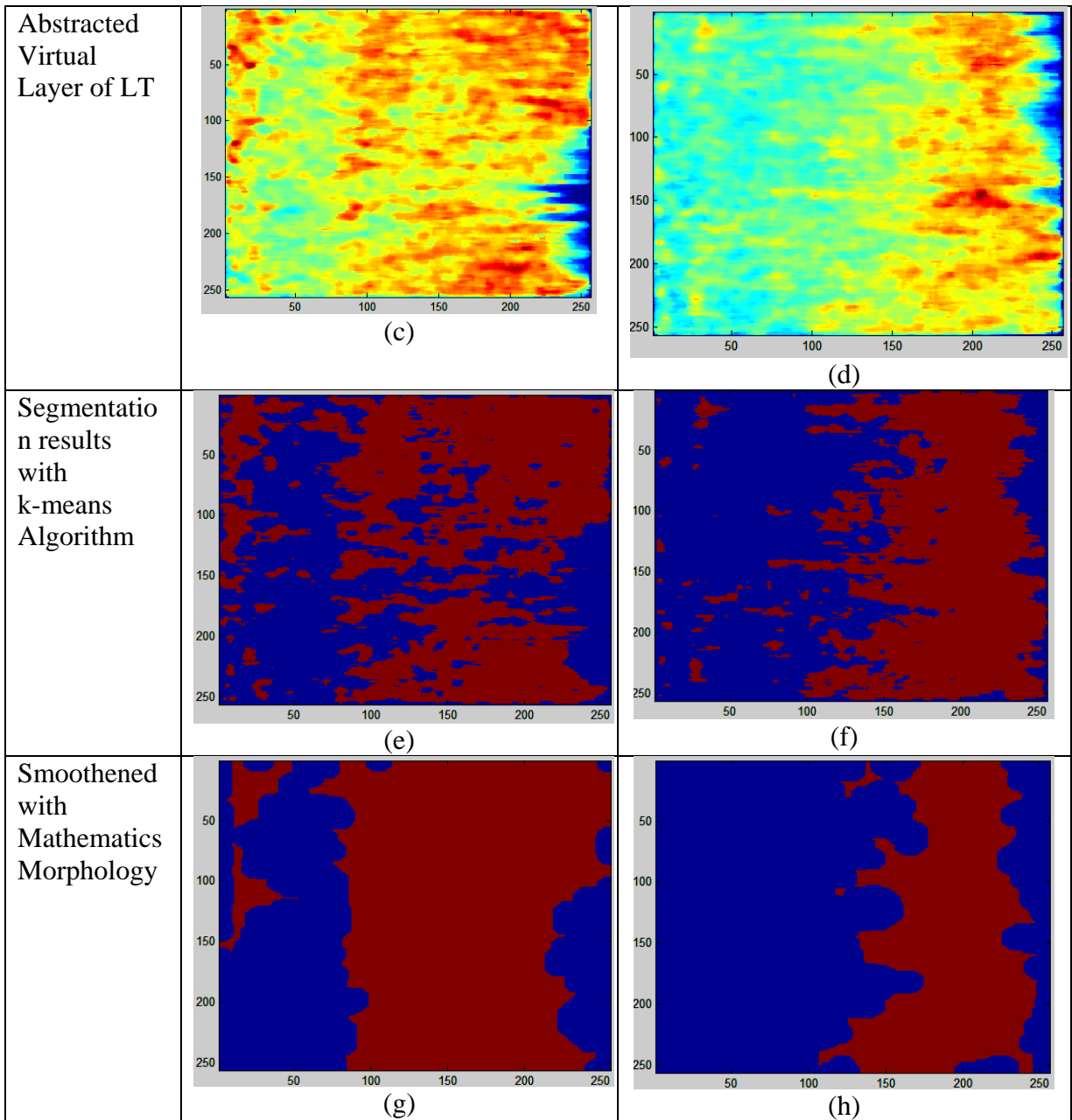


Figure 21. Continued

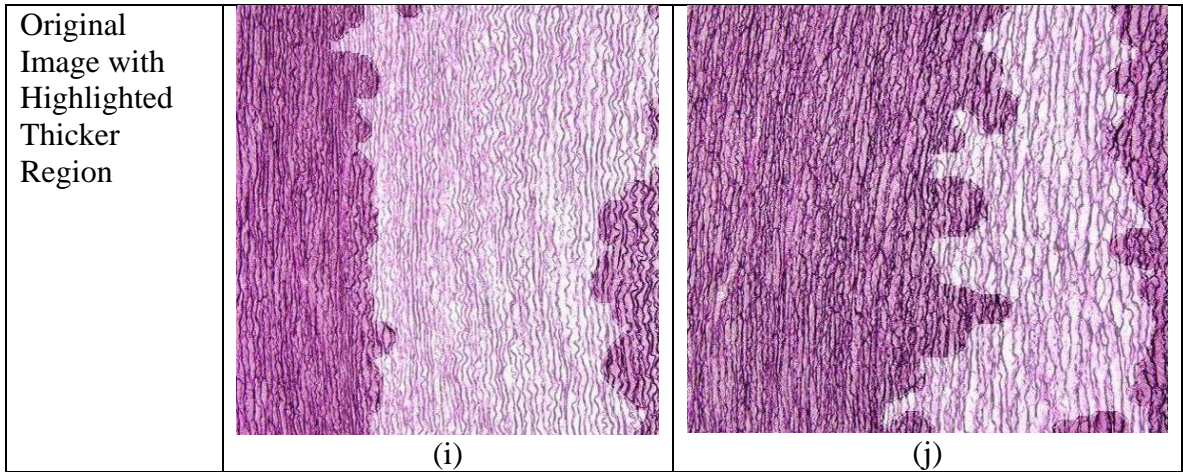


Figure 21. Continued

3.6 Statistics analysis and hypothesis test of LT and ILD based on virtual layer matrix

To analyze the morphology changes between NT and HT samples, I applied ANOVA [30] (analysis of variance) statistics to (1)averaged LT/ILD, (2)averaged VLM and (3)thickened area ratio of VLM. All following experiments are based on 13 NT and 19 HT samples. The F statistic was used to test the null hypothesis H_0 :

$$H_0: \mu_1 = \mu_2 = \dots = \mu_i, \quad (14)$$

where μ_i is the mean of sample i . I wanted to test whether or not there were significant differences between the measurement means at a significant level $\alpha = 0.1$. The test statistic α is the probability of exceeding the value of the test under the null hypothesis. The value labeled Prob > F in the last column of is often referred as the “P-value”.

In my first experiment, the averaged VLM of LT and ILD are compared, Figure 22. The averaged LTs decreased 9.5% from 6.3 to 5.7 pixels. The p-value is 0.2988. The ILD increased 20% from 13 to 15.6 pixels. And the p-value is 0.0014 which means there

is a significantly ILD increase. These two statistics analysis outcomes are consistent with above experiments.

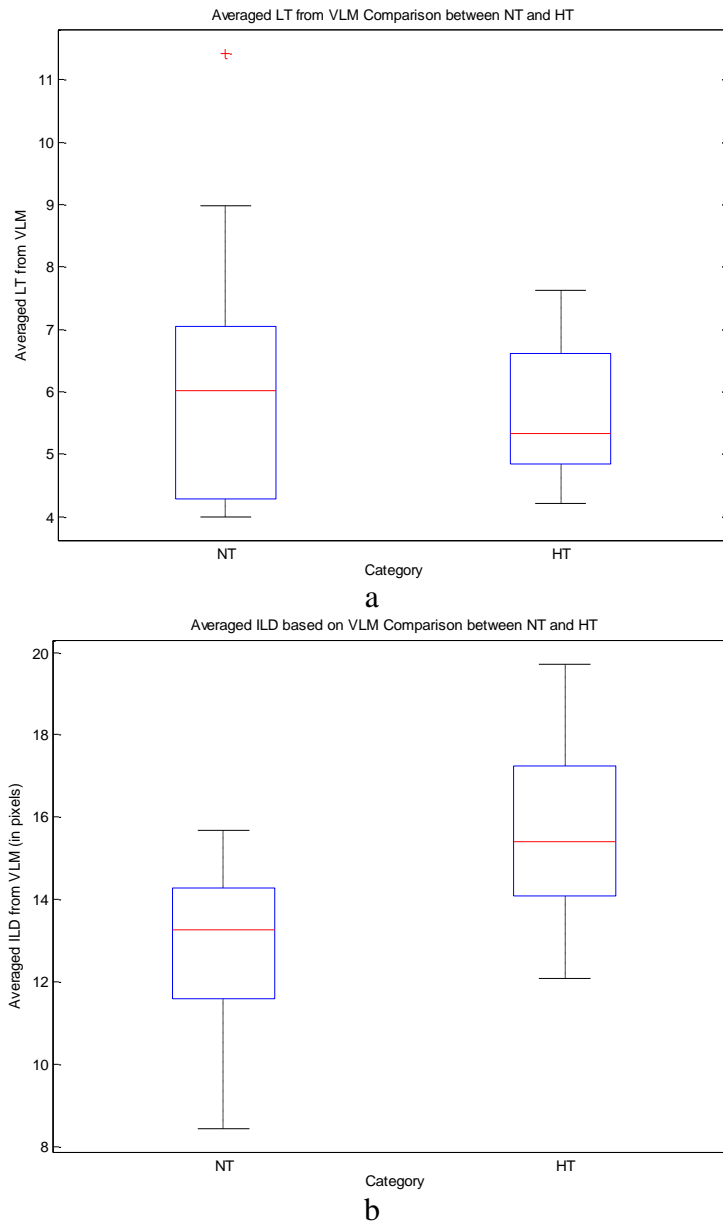


Figure 22. Averaged VLM boxplots of data from averaged LT/ILD values of VLM. Both computations include three categories: NT and HT aortic samples. X-axis shows the categories which NT are a normotensive samples, HT are hypertensive samples. X axis demonstrates the averaged VLM of LT/ILD. The middle line in each box is the median within each group. The upper and lower bound of each box is the lower (25%) and upper (75%) quartile.

In my second experiment, I want to analyze the thickened LT/ILD ratio in the wall segment, Figure 23. I defined the LT or ILD which is thicker than average to be thickened ones. The thickened LT ratio increased from 41.8% to 54.9% with 31.3% increase, and the thickened ILD ratio increased from 40.6% to 56.1% with 38.2% increase. The p-values of them are 0.1004 and 0.0573.

Summarizing all above statistics, I can conclude the following two key results:

Result 1: Averaged LT statistically decreased from NT to HT group.

Result 2: Averaged ILD statistically increased from NT to HT group.

Result 3: For thickened LT and ILD ratio analysis, both to them pronounces a significant increase from NT to HT at significant level 0.1

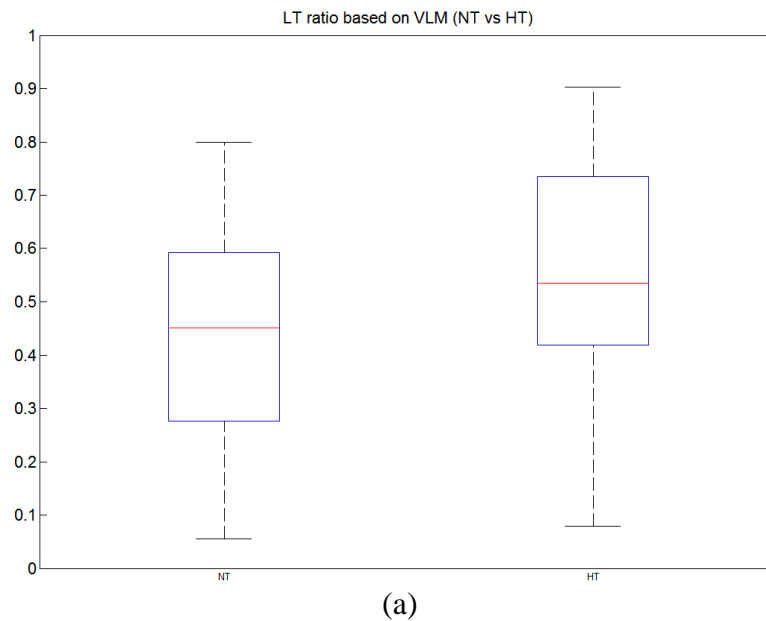


Figure 23. Averaged VLM boxplots of data of thickened (a) LT ratio and (b) ILD ratio. Both computations include three categories: NT and HT aortic samples. X-axis shows the categories which NT are normotensive samples, HT are hypertensive samples. Y axis demonstrates the thickened LT ratio (range from 0 to 1. The middle line in each box is the median within each group. The upper and lower bound of each box is the lower (25%) and upper (75%) quartile.

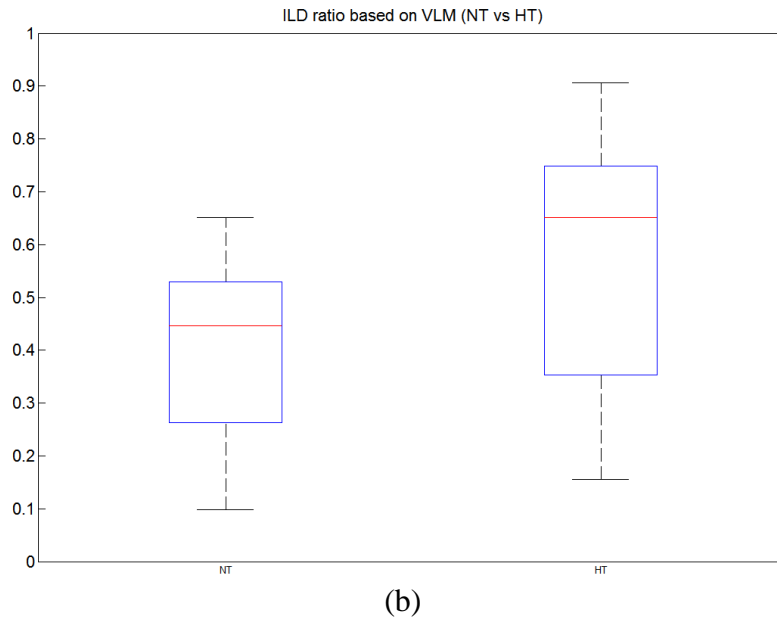


Figure 23. Continued

3.7 VLM analysis discussion

3.7.1 VLM statistics analysis and discussion

In my previous research [27, 35], I provided EL thickness and ILD in both 1D and 2D distribution mapping, provides information of LT or ILD in the radial direction. The values variations can be explained as LT/ILD average changes in the radial direction. But the averaged mean might smear the changes in the principal direction (which is perpendicular to the radial direction), lots of special information were lost. And some abnormal information might be prominent. That is the reason why the 1D distribution is not smooth at all. I then also try to use 2D distribution to provide more meaningfully information, such as. In, LT/ILD was categorized into three tiers. In the above-average thickness tier, LT of HT was significantly aggregated than that of NT.

But as the sparseness of the measurement, the LT aggregation phenomenon is not significantly displayed.

To overcome the limitation of these two methods, I will be able to map the EL thickness two-dimensional measurement to a highly-abstracted virtual layer mapping. The dimension of the target object was reduced from original image size, which is about thousands pixels in both direction, to a 256 by 256 matrix. By analyzing the segmentation results from above figures, it illustrates an obscured aggregated region which is close the intima layer of the aorta with hypertension. But in the normotensive vessels, this phenomenon is not significant. On the contrary, it illustrates a dispersed distribution. This observation is consistent with the related 1D LT distribution and my statistical hypothesis validation in section 2.4. The reason of the aggregation might because the intima layer will increase the speed of new-born cells to reduce the effects of hypertension.

To further highlight the significantly thicker region, I segmented the virtual layer of LT into two segments. In Figure 22 (g) and (h), the thicker regions are marked as red and thinner regions are blue. Then mathematics morphology operations: dilate and erode were applied to remove smaller regions, showing in figure d and i. In the last 2 figure e and j, I overlapped the segmentation results with the original images.

From the segmentation results, I will be able to conclude that LT distribution will illustrate a more aggregate phenomenon in hypertensive image than in normotensive one. This whole analysis process is fully automated with same parameters. It will be

very helpful to objectively differentiate the aorta walls into regions with different thickness.

In normotensive aorta, the EL thickness is statistically uniformly distributed. I proved this phenomenon in my previous work [35]. I also found out the EL thickness distribution does illustrate a non-uniformly distribution. But it is quite difficult to delineate this observation with naked eyes. With the mythology provided in this dissertation, I will be able to automatically extract the EL, calculate their thickness. It can semi-auto trace each single lamina, isolate lamina network thread by thread and finally generate an abstract representation: virtual layer. From the virtual layer, I are easier to find out the EL thickened areas. I can also compare the VL between normotensive and hypertensive data to further confirm my conclusion: the EL thickness in hypertension aorta is much more aggregated than in normotensive vessels.

3.7.2 Comparison to morphology thinning algorithm on lamina detection

Morphology Thinning (MT) algorithm is another feasible algorithm to obtain the EL structure information, especially when there are some noises in the aorta sample image. Furthermore, to obtain the skeleton of the EL, I have to choose a threshold which highly depends on the image quality. In my previous research, I was only focus on high-quality images. But to process relative low quality image or images with noises, morphology thinning algorithm might not be a good choice.

To illustrate the limitation of morphology thinning, two examples were listed as

Figure 24. In this comparison, I used a hard threshold 140 to binarized the grayscale image. Even though the original color image provides a good contrast, but when I convert the color image to grayscale, I am able to observe the much background noises and the rough boundary of the EL (marked as dotted circle in Figure 24). Under this circumstance, a hard threshold might provide a rough estimation of the ELs. Then, as the MT is highly depending on the binary image, MT will introduce many small branches and broken “lines”. All these outcome of MT might not provide clear and accurate LT distribution information. A length threshold might help to remove some noises and broken “lines”, but some useful globalize EL skeleton information might be lost as a compromise. And the parameter turning and signal-noise differentiation is still a challenge task.

To compare the MT with my Log-Gabor based searching algorithm with some manually picked starting points in Figure 24, I obtain the skeleton of the EL. Each starting points were highlighted with a yellow crossing. Each searching route was highlighted with different colors. It is easy to see that the Log-Gabor based searching algorithm can provide a more continuous and clear EL skeleton. Furthermore, because the manual picked starting points were intended chosen on the thicker lamina, those smaller “signal” would not be chosen in the VL analysis.

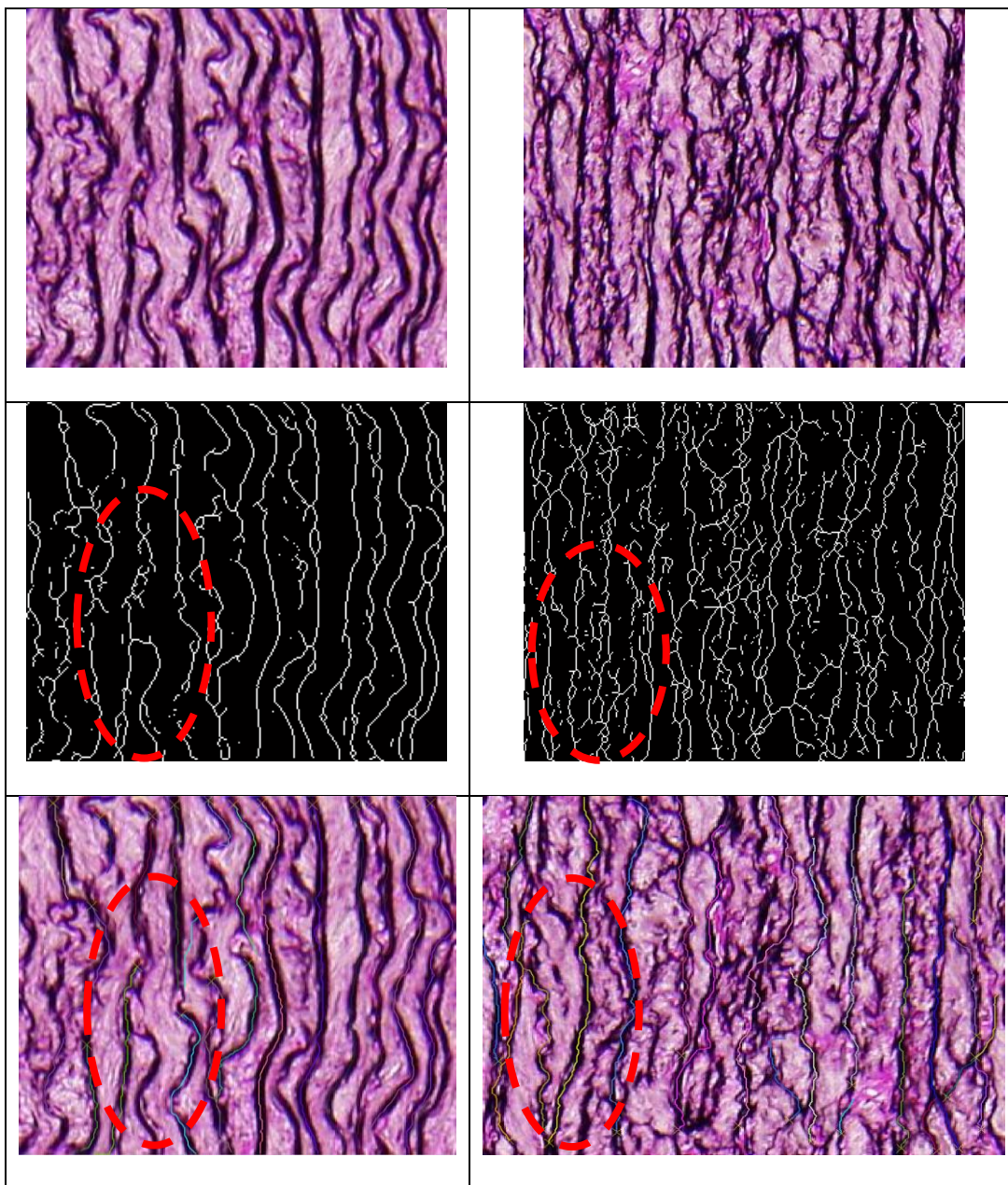
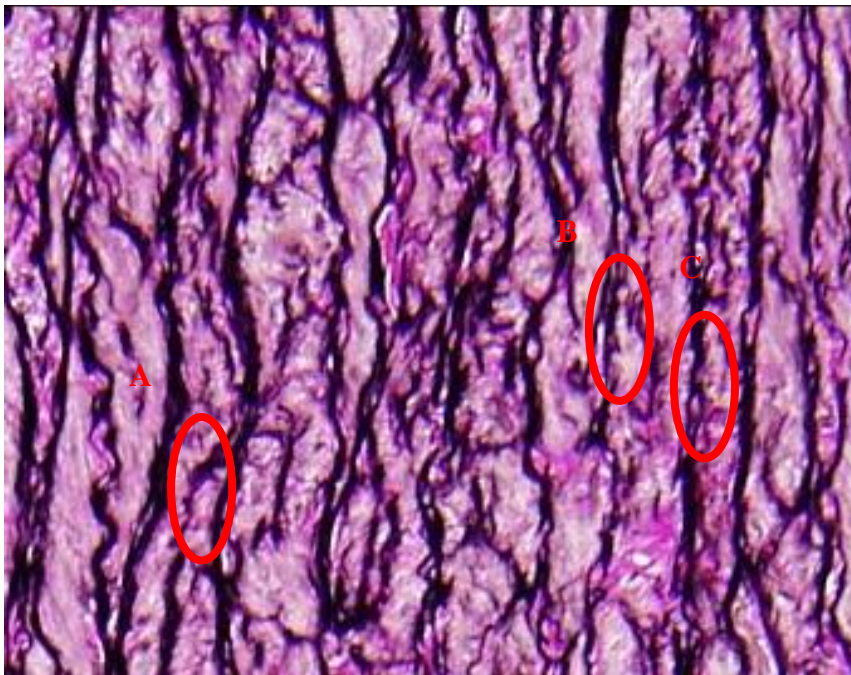


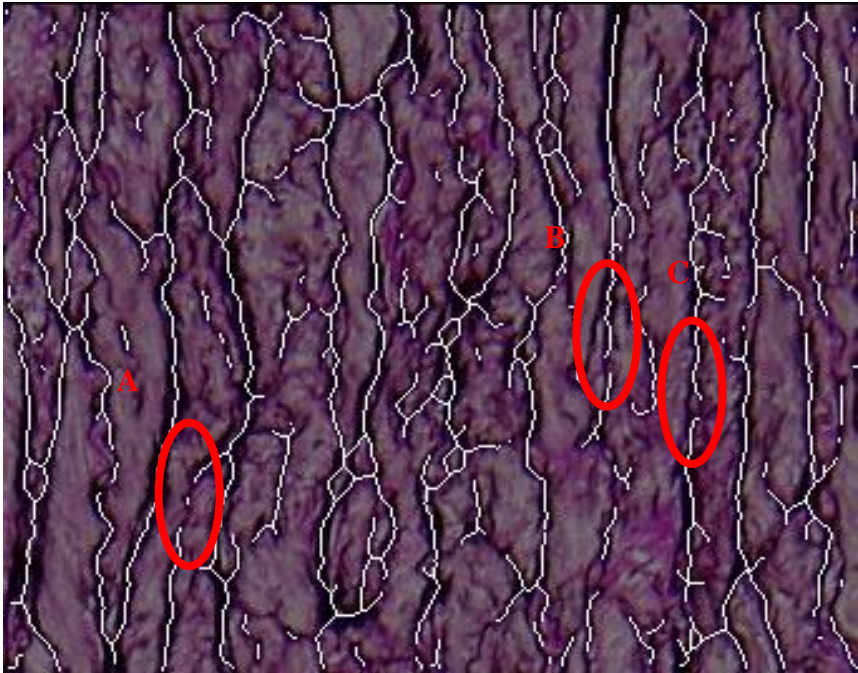
Figure 24. Two aorta images (first row), their EL maps obtained using a morphology thinning algorithm (second row), and ELs by LGF-based search using manually selected initial points. This example illustrates that the morphology thinning algorithm is susceptible to high frequency noise. It also suggests that the LGF-based search algorithm is robust to noise with an optimal set of initial points for the search routine.

Log-Gabor based algorithm can also deal with discontinued laminae. There are some samples might have blur contrasts or broken tissue. By directly applying thresholding method, there might be lots of broken parts. For example, in Figure 25, there are some ELs have a loose connection. By direction applying the threshold, some parts might be completely broken which is highlighted with red circles. But with LGF based method, those discontinued parts were connected.

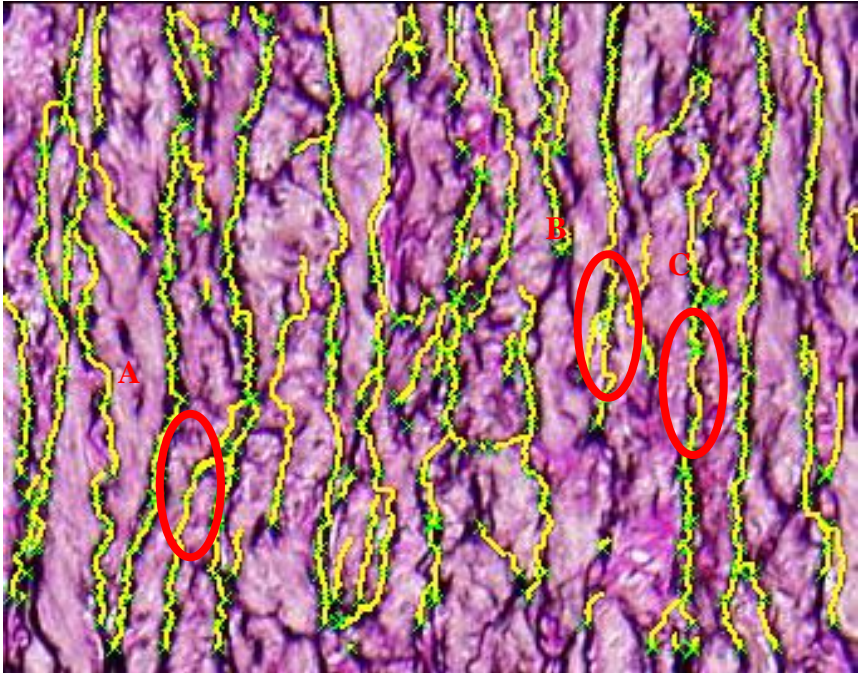


(a)

Figure 25. EL detection result comparison between morphology thinning algorithm and Log-Gabor Filter based algorithm. Three EL thread were chosen and marked as A, B and C respectively. From the original image, the ELs are continues. But with thresholding, the tissues are broken. In the orientation mapping, the flows of ELs are clearly continued. Thereafter, in my Log-Gabor based algorithm searching result, the EL tissues are connected.



(b)



(c)

Figure 25. Continued

CHAPTER IV

CONCLUSION

The normal aorta is the prototypical elastic artery; it is characterized by prominent circumferentially oriented concentric elastic laminae within the media. Two delimiting elastic laminae, together with the enclosed layer of smooth muscle cells and collagen fibers, constitute the lamellar unit, the basic biomechanical unit for elastic arteries [48]. Both the laminae thickness (LT) and inter-lamellar distance (ILD) are thought to be distributed evenly within in the media under physiologic conditions [8-10], but can become non-uniformly distributed under non-physiologic conditions, as, for example, in hypertension. Wolinsky and Glagov [49] analyzed 26 segments of rabbit aorta and reported that ILD are distributed uniformly at and above the diastolic pressure in healthy vessels. In contrast, Sans and Moragas [32] found that ILD are significantly greater in inner compared to outer regions of the media based on histological sections from 55 autopsy specimens (29 hypertensive patients and 26 controls), with regional variations being more marked in the hypertensive patients than in controls. Given the importance of such measurements, a fast, reliable, automated procedure would clearly be of great help in large scale biomechanical studies. Note, therefore, that Wolinsky and Glagov [49] measured LT and ILD by simply using a centimeter scale and photographic magnification of light and electron micrographs. The mean of four “eye-balled” values were used as the estimation. Similarly, Jaeckel and Simon [50] measured LT and ILD from digitized images using micrometers. With the help of a light video microscope and

a SAMBA 2005 automatic image analyzer, Charpiot et al. [51] manually drew radial lines across the media (from the lumen to the adventitia) and the elastic laminae intercepted by the line were identified and determined on the intensity profile to compute LT and ILD. See also [52].

To my knowledge, the approaches proposed by Sans and Moragas [32] and Jiang et al. [28] are the only two computer-based algorithms designed specifically for determining arterial LT and ILD, yet neither computed transmural distributions or performed regional analyses, which can provide more complete information about morphologic changes in cases such as the progression of hypertension. Nonetheless, note that after identifying elastic laminae by interactive thresholding, Sans and Moragas [32] performed morphological opening to evaluate LT and ILD with five or six different thickness values in multiple iterations. Starting from the smallest value, binarized laminae having a thickness less than the setting would be removed and labeled as the value. While they recognized the importance of aligning the elastic laminae with the orientation of the structuring element, their assumption of orthogonality to the elastic laminae may not always hold. Based on my evaluations using known synthetic data, misaligned elastic laminae can lead to overestimations of LT by their method. Moreover, the need for manual selection of the shape and size of the structural element renders calibration prone to error. Jiang et al. [28] developed a geometric algorithm to derive LT and ILD based on assumptions that laminae are nearly straight and aligned and that only small changes exist in thickness distributions. Such assumptions may not hold for some specimens during transient changes in early disease progression. Finally, most prior

work focused on small regions of the aortic cross-section without offering complete LT and ILD information across wall. There is, therefore, virtually no systematical study on the (non)-homogeneity of LT and ILD distributions across different areas. Using such small portions of whole cross-sections for study (e.g., LT and ILD analysis) was due, in part, to the prior lack of computing power and reliable computing algorithms.

The main contribution of this dissertation is the development and testing of a fully automated image analysis system that is capable of a broad range of analyses of elastic laminae within standard histological cross-sections of the arterial wall (e.g., metrics of importance such as LT, ILD, and FP-density). My solution scheme is accurate, robust to image variations, and fast; it uses as input a stained raw image and makes automated measurements with little to no parameter calibration. The system can also automatically assess the homogeneity or heterogeneity of measurements along the physiologic directions using hypothesis testing. This development also led to several important technical findings. Experimental results showed that both the LF (linear fitting) method and my RT (radon transform) method can align small images well. The main differences between these two methods, however, are that the RT-based approach does not require parameter adjustment while the LF-based approach is sensitive to parameter selection and is slower than RT for large images. Moreover, the RCBD (randomized complete block design) technique combined with an F -test was found to be a more cost effective method to assess homogeneity/heterogeneity of the LT and ILD than was piecemeal observations from a limited number of experiments [2]. Moreover, although global averages of point-wise measurements of LT or ILD in aortic cross-

sections may be adequate in some cases, a localized (e.g., window based) measurement technique is more appropriate in general. Otherwise, subtle information about transmural variations in LT or ILD, especially those associated with different stages of disease, could be lost. Whether manual [4, 8, 10, 11] or computer-based [6, 8, 28, 32], image analysis techniques should be applied to a broader range of aortic areas, not just a few selected areas.

On the basis of aforementioned observations, I made three different types of measurements: radially-oriented LT and ILD measurements, a two-dimensional expansion for LT, and also a two-dimensional measurement of FP-density for normotensive and hypertensive sections for side-by-side comparisons. As expected, localized structural changes can be detected by the region based measurement method, but such changes would be lost from global data aggregation techniques. Finally, with regard to the specific illustrative findings for normotensive (NT) and hypertensive (HT) porcine aorta, measurements in nearly stress-free configurations revealed potentially important increases in LT within the inner third of the media after 4 weeks of hypertension (Figure 7b). This is consistent with prior reports. Moreover, it appeared that this heterogeneity was due to the thicker, not thinner, sub-population of laminae (Figure 8), thus suggesting possible increased deposition within the inner wall rather than increased degradation within the outer wall in hypertension. The FP-density was found to be another interesting metric for elastin structure. Recall that Table 6 revealed that FP-density decreased monotonically with increased durations of hypertension – the phenomenon was not very pronounced during the first four weeks, but it increased

significantly at six and eight weeks: $\mu_{S,FP}$ was about 25% and 50% less than that for the surgical controls (SC), but $\mu_{L,FP}$ provided similar results. As a hypothesis, if lower FP densities imply more elastin tearing (less fractions), then a partial “healing process” could have served to reconnect some of the fragmented elastin during the first four weeks of hypertension. After six weeks, however, it appeared that any possible early reparative process was not sufficient to offset continued elastin tearing. More comprehensive studies are needed to test this and similar hypotheses.

My technique can also be applied to measure transmural distributions of other geometric parameters, including (1) elastic laminae area S_{EL} , (2) elastic laminae number n_{EL} , that is, elastic laminae skeleton count perpendicular to the principal direction, (3) elastic laminae intensity I_{EL} , that is, the grayscale value of an elastic laminae, (4) elastic laminae length l_{EL} relative to the length of a skeleton, (5) elastic laminae average length $\overline{l}_{EL} = l_{EL}/n_{EL}$, and (6) elastic laminae area ratio r_{EL} relative to the S_{EL} over detected interlamellar region area.

In conclusion, automatic identification of elastic laminae in standard histological arterial sections can be used as a fast and reliable screening tool to guide subsequent analyses, such as immunohistochemistry. Compared to conventional methods, my technique is the first to objectively quantify transmural metrics of importance for the elastic laminae. Illustrative results from normotensive and hypertensive porcine aorta show that such metrics can provide important regional contrasts as a function of disease. Hence, my system can be applied to a much broader range of applications wherein elastin damage, denaturation, or degradation are expected. It can be used, for example, to

quantify medial changes in balloon- or stent-induced restenosis, in Marfan syndrome, and in aging. Correlation of potential transmural gradients in these structural features with gradients in wall stress/strain or growth factors, cytokines, or proteases may provide further insight into disease progression and thereby possibly offer new insights into possible treatments.

REFERENCES

- [1] T. W. Fossum, W. I. Baltzer, M. W. Miller, M. Aguirre, D. Whitlock, P. Solter, L. A. Makarski, M. M. McDonald, M. Y. An, and J. D. Humphrey, "A novel aortic coarctation model for studying hypertension in the pig," *Journal of Investigative Surgery*, vol. 16, pp. 35-44, Jan 2003.
- [2] R. L. Gleason and J. D. Humphrey, "A mixture model of arterial growth and remodeling in hypertension: altered muscle tone and tissue turnover," *J Vasc Res*, vol. 41, pp. 352-363, Jul-Aug 2004.
- [3] R. L. Gleason and J. D. Humphrey, "Effects of a sustained extension on arterial growth and remodeling: a theoretical study," *J Biomech*, vol. 38, pp. 1255-1261, Jun 2005.
- [4] J. Gosline, M. Lillie, E. Carrington, P. Guerette, C. Ortlepp, and K. Savage, "Elastic proteins: biological roles and mechanical properties," *Philos Trans R Soc Lond B Biol Sci*, vol. 357, pp. 121-132, Feb 2002.
- [5] S. K. Karnik, B. S. Brooke, A. Bayes-Genis, L. Sorensen, J. D. Wythe, R. S. Schwartz, M. T. Keating, and D. Y. Li, "A critical role for elastin signaling in vascular morphogenesis and disease," *Development*, vol. 130, pp. 411-423, Jan 2003.
- [6] M. P. Jacob, "Extracellular matrix remodeling and matrix metalloproteinases in the vascular wall during aging and in pathological conditions," *Biomed Pharmacother*, vol. 57, pp. 195-202, Jul-Aug 2003.

- [7] M. Pezet, M. P. Jacob, B. Escoubet, D. Gheduzzi, E. Tillet, P. Perret, P. Huber, D. Quaglino, R. Vranckx, D. Y. Li, B. Starcher, W. A. Boyle, R. P. Mecham, and G. Faury, "Elastin haploinsufficiency induces alternative aging processes in the aorta," *Rejuvenation Res*, vol. 11, pp. 97-112, Feb 2008.
- [8] S. E. Greenwald, "Ageing of the conduit arteries," *J Pathol*, vol. 211, pp. 157-172, Jan 2007.
- [9] M. F. O'Rourke and J. Hashimoto, "Mechanical factors in arterial aging: a clinical perspective," *J Am Coll Cardiol*, vol. 50, pp. 1-13, Jul 2007.
- [10] S. M. Arribas, A. Hinek, and M. C. Gonzalez, "Elastic fibres and vascular structure in hypertension," *Pharmacol Ther*, vol. 111, pp. 771-791, Sep 2006.
- [11] H. C. Dietz and R. P. Mecham, "Mouse models of genetic diseases resulting from mutations in elastic fiber proteins," *Matrix Biol*, vol. 19, pp. 481-488, Nov 2000.
- [12] J. D. Humphrey and P. B. Canham, "Structure, properties, and mechanics of intracranial saccular aneurysms," *J Elast*, vol. 61, pp. 49-81, 2000.
- [13] D. A. Vorp, "Biomechanics of abdominal aortic aneurysm," *J Biomech*, vol. 40, pp. 1887-1902, 2007.
- [14] A. Krettek, G. K. Sukhova, and P. Libby, "Elastogenesis in human arterial disease: a role for macrophages in disordered elastin synthesis," *Arterioscler Thromb Vasc Biol*, vol. 23, pp. 582-587, Apr 1 2003.
- [15] F. Ganaha, K. Ohashi, Y. S. Do, J. Lee, K. Sugimoto, H. Minamiguchi, C. J. Elkins, D. Sameni, S. Modanlou, M. Ali, E. Y. Kao, M. A. Kay, J. M. Waugh, and M. D. Dake, "Efficient inhibition of in-stent restenosis by controlled stent-

- based inhibition of elastase: a pilot study," *J Vasc Interv Radiol*, vol. 15, pp. 1287-1293, Nov 2004.
- [16] M. A. Lillie and J. M. Gosline, "Tensile residual strains on the elastic lamellae along the porcine thoracic aorta," *J Vasc Res*, vol. 43, pp. 587-601, 2006.
- [17] T. Hou-Chun and H. Hsueh-Ming, "A novel approach for edge orientation determination based on pixel pair matching," in *ICIP*, Chicago, IL, 1998, pp. 545-549.
- [18] A. Sourice, G. Plantier, and J. L. Saumet, "Autocorrelation fitting for texture orientation estimation," in *ICIP*, Barcelona, Spain, 2003, pp. 281-284.
- [19] F. Deguillaume, S. Voloshynovskiy, and T. Pun, "A method for the estimation and recovering from general affine transforms in digital watermarking applications," in *SPIE*, San Jose, CA, 2002, pp. 313-322.
- [20] J. Bigun, G. H. Granlund, and J. Wiklund, "Multidimensional orientation estimation with applications to texture analysis and optical-flow," *IEEE Transactions on Pattern Analysis and Machine Intelligence*, vol. 13, pp. 775-790, Aug 1991.
- [21] D. V. S. Chandra, "Target orientation estimation using Fourier energy spectrum," *IEEE Transactions on Aerospace and Electronic Systems*, vol. 34, pp. 1009-1012, Jul 1998.
- [22] E. Magli, L. Lo Presti, and G. Olmo, "A pattern detection and compression algorithm based on the joint wavelet and Radon transform," in *13th International Conference on Digital Signal Processing*, Santorini, Greece, 1997, pp. 559-562.

- [23] F. Michelet, C. Germain, P. Baylou, and J. P. da Costa, "Local multiple orientation estimation: isotropic and recursive oriented network," in *ICPR*, Cambridge, England, 2004, pp. 712-715.
- [24] R. C. Gonzalez and R. E. Woods, *Digital image processing*, 2nd ed. Upper Saddle River, NJ: Prentice Hall, 2002.
- [25] T. Pavlidis, "A thinning algorithm for discrete binary images," *Computer Graphics and Image Processing*, vol. 13, pp. 142-157, 1980.
- [26] L. Lam, S. W. Lee, and C. Y. Suen, "Thinning methodologies - a comprehensive survey," *IEEE Transactions on Pattern Analysis and Machine Intelligence*, vol. 14, pp. 869-885, Sep 1992.
- [27] H. Xu, J.-J. Hu, J. D. Humphrey, and J.-C. Liu, "Modeling and measurement of elastic laminae in arteries," in *ISBI*, Arlington, VA, 2006, pp. 626-629.
- [28] C. F. Jiang, A. P. Avolio, and B. G. Celler, "Quantification of the elastin lamellar structure in histological sections of the arterial wall by image analysis," *Journal of Computer Assisted Microscopy*, vol. 7, pp. 47-55, 1995.
- [29] P. H. Gregson, Z. Shen, R. C. Scott, and V. Kozousek, "Automated grading of venous beading," *Computers and Biomedical Research*, vol. 28, pp. 291-304, Aug 1995.
- [30] A. C. Tamhane and D. D. Dunlop, *Statistics and data analysis: from elementary to intermediate*. Upper Saddle River, NJ: Prentice Hall, 1999.
- [31] R. O. Kuehl, *Design of experiments: statistical principles of research design and analysis*, 2nd ed. Pacific Grove, CA: Duxbury Press, 1999.

- [32] M. Sans and A. Moragas, "Mathematical morphologic analysis of the aortic medial structure - biomechanical implications," *Analytical and Quantitative Cytology and Histology*, vol. 15, pp. 93-100, Apr 1993.
- [33] F. Zana and J. C. Klein, "A multimodal registration algorithm of eye fundus images using vessels detection and Hough transform," *IEEE Transactions on Medical Imaging*, vol. 18, pp. 419-428, May 1999.
- [34] F. Laliberte and L. Gagnon, "Registration and fusion of retinal images - An evaluation study," *IEEE Transactions on Medical Imaging*, vol. 22, pp. 661-673, May 2003.
- [35] H. Xu, J.-J. Hu, J. D. Humphrey, and J.-C. Liu, "Automated measurement and statistical modelling of elastic laminae in arteries," *Computer Methods in Biomechanics and Biomedical Engineering*, vol. 13, pp. 749-763, 2010.
- [36] P. Yao, J. Li, X. Ye, Z. Zhuang, and B. Li, "Iris recognition algorithm using modified log-gabor filters," presented at the ICPR, Hong Kong, 2006.
- [37] D. H. Dunn, W.E. , "Optimal gabor filters for texture segmentation," *IEEE Transactions on Image Processing*, vol. 4, pp. 947-964, July 1995.
- [38] A. Teuner, O. Pichler, and B. J. Hosticka, "Unsupervised texture segmentation of images using tuned matched Gabor filters," *IEEE Transactions on Image Processing*, vol. 4, pp. 863-870, June 1995.
- [39] J. G. Daugman, "Uncertainty relation for resolution in space, spatial frequency, and orientation optimized by two-dimensional visual cortical filters," *J Opt Soc Am A*, vol. 2, pp. 1160-1169, Jul 1985.

- [40] D. J. Field, "Relations between the statistics of natural images and the response properties of cortical cells," *Journal of the Optical Society of America. A*, vol. 4, pp. 2379-2394, 1987.
- [41] X. Gao, F. Sattar, and R. Venkateswarlu, "Multiscale corner detection of gray level images based on log-gabor wavelet transform," *IEEE Transactions on Circuits and Systems for Video Technology*, vol. 17, pp. 868-875, 2007.
- [42] W. Wang, J. Lia, F. Huanga, and H. Feng, "Design and implementation of log-gabor filter in fingerprint image enhancement," *Pattern Recognition Letters*, vol. 29, pp. 301-308, February 2008 2008.
- [43] S. Geuna, S. Cardillo, and M. G. Giacobini-Robecchi, "Smooth muscle cell hypertrophy and hyperplasia in the partially obstructed gut of the rat: a quantitative evaluation," *Acta Anat (Basel)*, vol. 163, pp. 69-74, 1998.
- [44] P. Kovesei, "Phase congruency detects corners and edges," presented at the The Australian Pattern Recognition Society Conference: DICTA, Sydney, 2003.
- [45] T. S. Lee, "Image representation using 2D Gabor wavelets," *IEEE Transactions on Pattern Analysis and Machine Intelligence*, vol. 18, pp. 959-971, 1996.
- [46] S. L. G. d. Oliveira and J. T. d. Assis, "A methodology for identification of fingerprints based on Gabor filter," *IEEE Latin America Transactions*, vol. 4, pp. 1-6, 2006.
- [47] J. B. MacQueen, "Some methods for classification and analysis of multivariate observation," in *Proceedings of fifth Berkeley Symposium on Mathematical Statistics and Probability*, Berkeley, CA, 1967, pp. 281-297.

- [48] J. M. Clark and S. Glagov, "Transmural organization of the arterial media - the lamellar unit revisited," *Arteriosclerosis*, vol. 5, pp. 19-34, 1985.
- [49] H. Wolinsky and S. Glagov, "Structural basis for the static mechanical properties of aortic media," *Circulation Research*, vol. 14, pp. 400-413, 1964.
- [50] M. Jaeckel and G. Simon, "Altered structure and reduced distensibility of arteries in Dahl salt-sensitive rats," *Journal of Hypertension*, vol. 21, pp. 311-319, Feb 2003.
- [51] P. Charpiot, A. Bescond, T. Augier, C. Chareyre, M. Fraterno, P. H. Rolland, and D. Garcon, "Hyperhomocysteinemia induces elastolysis in minipig arteries: structural consequences, arterial site specificity and effect of captopril-hydrochlorothiazide," *Matrix Biol*, vol. 17, pp. 559-574, Dec 1998.
- [52] D. P. Sokolis, H. Boudoulas, N. G. Kavantzias, N. Kostomitsopoulos, E. V. Agapitos, and P. E. Karayannacos, "A morphometric study of the structural characteristics of the aorta in pigs using an image analysis method," *Anat Histol Embryol*, vol. 31, pp. 21-30, Feb 2002.

VITA

Hai Xu received his B.S. degree in electrical engineering and automation from Tsinghua University, Beijing, China in July 1998. From 2000 to 2002, he studied at Clemson University on his M.S. degree of electrical and computer engineering.

Hai Xu started working toward his Ph.D. degree in computer engineering at Texas A&M University in August 2002, under the supervision of Dr. Jyh-Charn Liu. His research areas of interest include biomedical image processing, pattern recognition, and statistical modeling and analysis. His permanent address is: Department of Computer Science, Texas A&M University, College Station, TX, 77843-3112.